Engineering Fracture Mechanics 336 (2026) 111931

Contents lists available at ScienceDirect

Engineering Fracture Mechanics

journal homepage: www.elsevier.com/locate/engfracmech

Concrete fatigue propagation from material to structure: Multiscale validation of a thermodynamically based discrete model on prisms and prestressed beams

Mario Aguilar [a,*], Miroslav Vořechovský [b], Abedulgader Baktheer [c], Rostislav Chudoba [a]

[a] Center for Structural Concrete Physics, RWTH Aachen University, Im Süsterfeld 9, 52072 Aachen, Germany
[b] Institute of Structural Mechanics, Brno University of Technology, Veveří 95, 602 00 Brno, Czech Republic
[c] Institute of Mechanics and Computational Mechanics, Leibniz Universität Hannover, 30167 Hannover, Germany

ARTICLE INFO

Keywords:
Concrete
Fatigue fracture
Constitutive modeling
Lattice discrete particle model
Anisotropic damage
Plasticity
Thermodynamics

ABSTRACT

Fatigue assessment of concrete structures relies predominantly on empirical evidence from uniaxial cylinder tests, codified into structural design rules. Several continuum damage-plasticity models have been developed to capture fatigue-induced dissipative mechanisms. However, they do not explicitly resolve how damage propagates through the aggregate skeleton and translates into structural behavior. This study addresses this gap by integrating a thermodynamically based inter-aggregate constitutive law into a lattice discrete particle model that explicitly represents mesoscale concrete heterogeneity. The thermodynamic formulation inherently decomposes dissipated energy into contributions from distinct degradation mechanisms, enabling mechanism-specific fatigue characterization. The model is calibrated using macroscopic characteristics of monotonic and fatigue response of prisms under compression and validated against prestressed beam experiments under variable-amplitude fatigue loading. Simulations reproduce experimental trends of fatigue response in prestressed beams, revealing two key findings: (i) the obtained Sparks–Menzies relation persists across material and structural scales; (ii) damage dissipation emerges as a scale-consistent, load-level-independent indicator of fatigue capacity within a given stress configuration, offering a physically grounded alternative to empirical design criteria. The present high-fidelity model provides the basis for resolving the transition from meso-scale material behavior to macroscopic structural response, and establishes a foundation for future coarse-graining and time-scale acceleration strategies required for large structures and long fatigue lives.

1. Introduction

Concrete fatigue has emerged as a critical area of research, driven by the increasing demand for high-performance reinforced concrete (RC) structures in modern engineering applications [1–5]. Applications such as slender, prestressed wind turbine towers and high-speed rail infrastructure rely on the ability of concrete to endure repeated loading with a substantially increased number of up to 10^7 loading cycles during their service life. As structural designs evolve toward higher material utilization, accurately

* Corresponding author.
E-mail address: maguilar@imb.rwth-aachen.de (M. Aguilar).

https://doi.org/10.1016/j.engfracmech.2026.111931
Received 12 August 2025; Received in revised form 11 January 2026; Accepted 8 February 2026
Available online 9 February 2026
0013-7944/© 2026 The Authors. Published by Elsevier Ltd. This is an open access article under the CC BY license (http://creativecommons.org/licenses/by/4.0/).

Nomenclature

$\boldsymbol{\alpha}$	Kinematic hardening state variable
$\boldsymbol{\varepsilon}$	Strain vector
$\boldsymbol{\sigma}$	Stress vector
$\boldsymbol{\sigma}^p$	Plastic stress vector
$\tilde{\boldsymbol{\sigma}}$	Effective stress vector
$\boldsymbol{\theta}$	Rotation vector
$\boldsymbol{n}_{\mathrm{N}}$	Facet normal vector
$\boldsymbol{n}_{\mathrm{T}}$	Facet tangential vector
$\boldsymbol{q}$	Kinematic vector
$\boldsymbol{u}$	Displacement vector
$\boldsymbol{u}^p$	Plastic displacement vector
$\boldsymbol{X}$	Back stress vector
$\boldsymbol{x}$	Position vector
$\boldsymbol{f}$	Force vector
$\boldsymbol{m}$	Moment vector
$\boldsymbol{p}$	Stress resultants vector
$\boldsymbol{\mathcal{E}}$	State variables vector
$\boldsymbol{\mathcal{S}}$	Thermodynamic forces vector
$\boldsymbol{\Phi}$	Flow direction vector
η	Damage interaction parameter
γ	Kinematic hardening modulus
λ	Plastic multiplier
$\mathcal{D}$	Energy dissipation
$\mathcal{U}$	Free energy
$\mathcal{W}$	Work
ω	Damage state variable
ψ	Helmholtz free energy function
ρ	Material density
φ	Non-associative flow potential
c	Damage accumulation exponent
E_{N}	Normal elastic modulus
E_{T}	Tangential elastic modulus
f	Elastic threshold
K	Isotropic hardening modulus
m	Pressure sensitivity parameter
N	Cycle
N_{f}	Cycles to failure
r	Damage rate exponent
S	Damage energy rate scaling parameter
$S_{\max}$	Upper bound of fatigue loading
$S_{\min}$	Lower bound of fatigue loading
Y	Energy release rate
Z	Isotropic hardening stress
z	Isotropic hardening variable
DIC	Digital image correlation
F	Applied external force
FOS	Fiber optic sensor
LS	Loading scenario
LVDT	Linear variable differential transformer

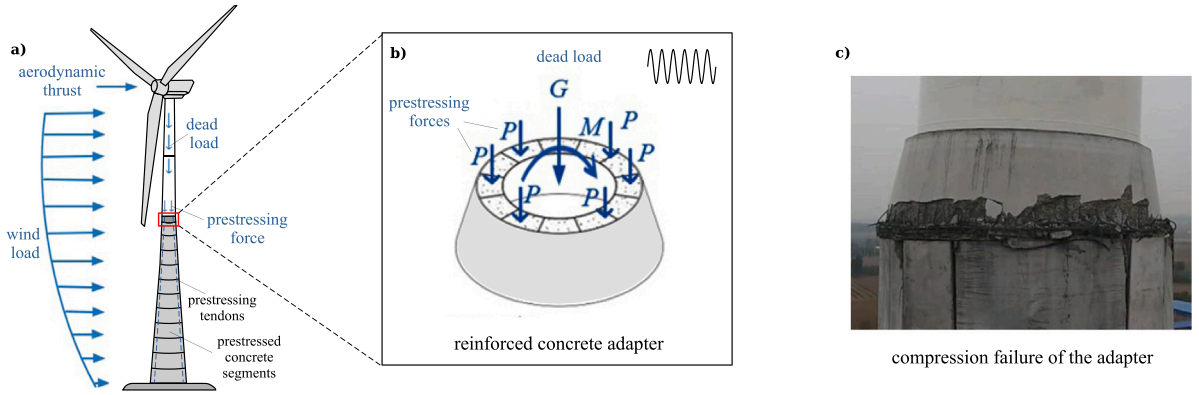


Fig. 1. Illustration of stress configurations in wind power plants, adapted from [30]: (a) Hybrid tower of wind power plants; (b) Load configuration in the reinforced concrete adapter; (c) Example of compression failure of the RC adapter.

assessing fatigue behavior — particularly under compressive loading — has become crucial for ensuring the durability and safety of critical infrastructure [6,7].

The composite nature of concrete, characterized by aggregates, cement paste, and interfacial transition zones (ITZs), introduces a level of heterogeneity that increases the demands on the comprehensive and rigorous formulation of the fatigue models. While experimental studies have made significant progress in characterizing fatigue properties [8–10], recent research has expanded to investigate a range of additional factors influencing fatigue performance. These include the effects of loading frequency and temperature [11–14], moisture content [15–17], multiaxial stress states [18–20], types of loading [21–23], and loading sequences with variable amplitude [24–29]. Despite these advances, existing design codes remain limited in their ability to address the complex loading scenarios and multiaxial stress states present in real-world structures.

Most codes rely on simplified empirical approaches based on uniaxial S-N curves, which do not account for critical phenomena such as triaxial stress redistribution or the role of microstructural interactions. For example, hybrid towers of wind turbines experience high compressive triaxial stresses, particularly in the reinforced concrete sections right below the steel tower exposed to forces schematically depicted in Fig. 1. Furthermore, the assumption of the linear damage accumulation hypothesis underlying the Palmgren–Miner rule [31,32] contradicts empirical evidence showing nonlinear effects [24–26].

To address these limitations, and to further interpret experimental results, various numerical modeling approaches have been developed. For tensile fatigue, cohesive zone elements are commonly used to simulate crack propagation under cyclic and mixed-mode loading conditions [33–37]. These methods are particularly effective for capturing discrete crack initiation and growth. To capture fatigue-induced tri-axial stress redistribution in the process zone of a tensile crack and its role in concrete fatigue, a successful application of the microplane framework has been presented in [38].

For compressive fatigue, classical phenomenological tensorial models within the damage-plasticity framework have been widely adopted [39–42]. These models are computationally efficient and capable of reproducing macroscopic phenomena such as Wöhler (S-N) curves and fatigue creep behavior [43]. However, simple models often overlook that compressive fatigue in concrete is predominantly governed by diffuse microcracking and pronounced local triaxial stress redistribution. Advanced models, such as the microplane model MS1 [44], have incorporated triaxial stress redistribution to better capture compressive fatigue mechanisms. Nevertheless, macroscopic models like MS1 operate within a continuum framework, averaging material behavior and neglecting mesostructural phenomena, such as aggregate interlock and localized crack interactions.

Mesoscale models offer a complementary approach by explicitly resolving the heterogeneity of concrete. These models enable detailed representation of crack evolution, stress redistribution, and fatigue-induced damage mechanisms under complex loading scenarios [45–47]. By providing higher resolution of the material structure, mesoscale models can yield more accurate predictions of fatigue life and offer deeper insight into damage progression.

The Lattice Discrete Particle Model (LDPM) [47–51] is a discrete computational approach based on the rigid body-spring concept [52]. It has emerged as one of the most effective frameworks for simulating the mechanical behavior of conventional concrete under a wide range of loading conditions. In LDPM, the concrete mesostructure is discretized into aggregate particles represented by nodes located at their centroids. Interfacial constitutive laws between aggregates model the behavior between aggregates [48,53]. The constitutive model incorporates enriched interactions to accurately capture triaxial stress states, enabling simulation of concrete responses across diverse loading scenarios—from uniaxial tension and compression to general triaxial stress conditions. LDPM has been extended to account for time-dependent phenomena, such as creep and rate effects, through the use of an explicit dynamic solver [54,55]. The versatility of LDPM has been demonstrated in applications spanning both quasi-static and dynamic loading regimes. For instance, it has been successfully applied to simulate projectile penetration through reinforced concrete slabs. More recently, LDPM has been employed to model the failure of 3D-printed thin-shell dome structures designed for extraterrestrial habitation [56,57], showcasing its adaptability to advanced engineering challenges.

However, when it comes to cyclic loading and fatigue, the existing LDPM-based approaches are sparse and often lack critical features necessary for capturing fatigue degradation under subcritical loads. Initial studies have explored crack propagation under lateral cyclic loading [58], and others have focused on modeling post-peak cyclic behavior [59]. Yet, these implementations typically do not incorporate explicit fatigue damage accumulation mechanisms, which restricts their predictive capability under prolonged cyclic or fatigue loading conditions. Attempts to address concrete fatigue under compression within the discrete element modeling framework have introduced simplified constitutive formulations to model progressive stiffness degradation [60–62]. While these approaches offer valuable insights, they lack a thermodynamic foundation and are limited in their applicability to general loading paths and complex stress states.

To address these limitations, the present work introduces a thermodynamically based LDPM-based fatigue model grounded in a unified constitutive hypothesis for fatigue damage evolution [63,64]. Building upon prior developments validated within the microplane framework [18,44], the proposed model formulates damage accumulation at the inter-aggregate level, driven by the evolution of inelastic strains. This mechanism enables the explicit representation of microstructural fatigue degradation, extending LDPM's applicability to realistic fatigue scenarios. By integrating microstructural heterogeneity with a physically motivated fatigue-degradation law, the model provides a more robust platform for virtual testing and complements experimental investigations. Ultimately, this advancement opens the door to multiscale modeling strategies, where microscale degradation mechanisms inform the macroscopic fatigue performance of concrete structures. Such a refined model can substantially enhance our understanding of the dissipative mechanisms governing the fatigue behavior of cementitious materials. In the long run, it has the potential to facilitate the design of durable and sustainable materials, supporting efficient resource usage and long-term structural resilience.

In addition to developing a mesoscale lattice discrete particle model, this study aims to bridge the gap between material-level characterization and structural-level fatigue behavior in concrete. While conventional compression cylinder tests offer valuable data on local fatigue properties under idealized uniaxial conditions, they fail to capture the complex stress redistributions that occur in real structural components. By numerically reproducing the fatigue degradation in prestressed four-point bending tests [65–67], which features non-uniform stress states, the LDPM simulations enable detailed analysis of spatial stress redistribution and damage evolution across multiple material zones. A key focus is placed on evaluating the energy dissipation associated with the fatigue process, which offers deep insights into the underlying damage mechanisms and their impact on global structural performance. This approach provides a profound insight into the transition from localized fatigue damage to global structural degradation, supporting more accurate lifetime prediction and advancing the design of fatigue-resistant concrete structures.

The paper is organized as follows: Section 2 provides an overview of the lattice discrete particle model, establishing the fundamental computational framework reviewing the applied mesoscale discretization of the material structure and inter-aggregate kinematics. Section 3 presents the applied thermodynamic formulation for inter-aggregate degradation behavior along with the description of the quantification of the breakdown of energy dissipation attributed to the individual inelastic mechanisms. Section 4 focuses on the model calibration using existing data on uniaxial monotonic and fatigue behavior of concrete. Section 5 provides structural-scale validation of the model using the calibrated material model and Section 6 discusses the relevance of the results in the light of existing engineering design concepts for concrete fatigue assessment.

2. Overview of lattice discrete particle model

The lattice discrete particle model (LDPM) solver is employed for an explicit simulation of the mesostructure of concrete [47,68]. The model represents the material as a system of particles with translational and rotational degrees of freedom. Rigid particles represent larger aggregates with surrounding cement matrix; smaller aggregates are omitted, their role being merged into the constitutive laws on contacts of the larger rigid particles.

Spatial domain discretization. The specimen or structural domain is first defined in physical space, and each aggregate piece is idealized as a sphere whose diameter is drawn from a prescribed granulometric law which reduces to the Fuller curve. The rigid particles are distributed throughout the domain by randomly placing them such that they do not overlap, maintain a minimum distance from the external boundaries, and satisfy a lower bound on the center-to-center spacing in terms of their radii, and then generate a tetrahedral mesh via the Delaunay algorithm applied to the particle centroids. Each resulting tetrahedron encloses exactly four particles at its vertices [45]. In the classical LDPM approach, every tetrahedron is further subdivided into twelve triangular facets, which serve as the interaction surfaces (integration points) between particles. This tessellation is constructed as follows (see Fig. 2, middle):

- Edge-points: Place one point on each of the six tetrahedral edges.
- Face-points: Place one point on each of the four triangular faces.
- Tet-point: Place a single point at the tetrahedron's barycenter.

By connecting each edge-point to the two adjacent face-points and to the tet-point, one obtains twelve non-overlapping triangles whose union exactly covers the original tetrahedron. Gathering all facets that touch a given particle yields a convex polyhedral cell around that particle (Fig. 2). Although one can simplify the kinematics by treating each Delaunay edge as a two-particle "strut" and assigning it an interaction area via a Voronoi tessellation (or power tessellation known also as Laguerre tessellation), this edge-only discretization neglects volumetric effects under confinement. For simulations dominated by high confining stresses — as in cyclic compression of prestressed concrete beams — such volumetric coupling is essential. Hence, we retain the full four-particle tetrahedral interactions with twelve facets per tetrahedron. In our framework, these facets define the localization zones through

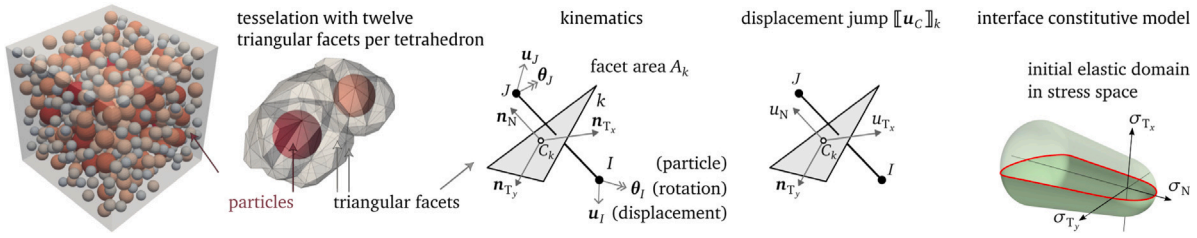


Fig. 2. LDPM model used. From the left: placement of particle centers, tesselation of volume, kinematics for each mechanical element associated with a triangular facet, displacement jump and the corresponding strain components and sketch of the elastic domain of the interface constitutive model.

which interaction forces (and damage) propagate, exactly as in the original LDPM formulation [45]. All these steps, from aggregate generation to mesh construction and quality control, are carried out using the MARS LDPM solver [68,69].

The kinematics of the model is provided by rigid-body motion of the particles, which results in displacement jumps between them.

Kinematics. The displacement $\boldsymbol{u}$ of an arbitrary point $\boldsymbol{x}$ within a rigid body can be expressed in terms of the displacement $\hat{\boldsymbol{u}}_K$ and rotation and the rotations $\hat{\boldsymbol{\theta}}_K$ of the reference node with coordinates $\hat{\boldsymbol{x}}_K$ as [45]

$$\boldsymbol{u}(\boldsymbol{x}) = \hat{\boldsymbol{u}}_K + \hat{\boldsymbol{\theta}}_K \times (\boldsymbol{x} - \hat{\boldsymbol{x}}_K), \text{ i.e., } \begin{Bmatrix} u_1 \\ u_2 \\ u_3 \end{Bmatrix} = \underbrace{\begin{bmatrix} 1 & 0 & 0 & 0 & x_3 - \hat{x}_{K3} & \hat{x}_{K2} - x_2 \\ 0 & 1 & 0 & \hat{x}_{K3} - x_3 & 0 & x_1 - \hat{x}_{K1} \\ 0 & 0 & 1 & x_2 - \hat{x}_{K2} & \hat{x}_{K1} - x_1 & 0 \end{bmatrix}}_{\boldsymbol{A}_K(\boldsymbol{x})} \cdot \underbrace{\begin{Bmatrix} \hat{u}_{K1} \\ \hat{u}_{K2} \\ \hat{u}_{K3} \\ \hat{\theta}_{K1} \\ \hat{\theta}_{K2} \\ \hat{\theta}_{K3} \end{Bmatrix}}_{\boldsymbol{q}_K{}^{\mathsf{T}} = [\hat{\boldsymbol{u}}_K{}^{\mathsf{T}} \mid \hat{\boldsymbol{\theta}}_K{}^{\mathsf{T}}]}, \tag{1}$$

where the subscripts 1, 2, and 3 refer to the three coordinate directions. In this description of rigid body motion, small deformations and rotations are assumed. Consider two rigid bodies, I and J and their common contact facet k with the centroid node C_k, as illustrated in Fig. 2. Assuming arbitrary displacements and rotations of particles I and J, the displacements $(\boldsymbol{u}_{CJ}, \boldsymbol{u}_{CI})$ of the point C relative to I and J are obtained using Eq. (1) by substituting $\boldsymbol{x} = \boldsymbol{x}_C$ and $K = I$, and $K = J$, respectively. The difference between the displacements from both sides of the contact facet

$$[\![\boldsymbol{u}_C]\!] = \boldsymbol{u}_{CJ} - \boldsymbol{u}_{CI} \tag{2}$$

expresses the displacement jump vector between rigid particles I and J at the centroid of the contact facet. The transformation of the jump to the local coordinates of the facet k is performed using the orthonormal basis

$$[\![\boldsymbol{u}_C]\!]_k = \boldsymbol{T}_k \cdot [\![\boldsymbol{u}_C]\!], \quad \boldsymbol{T}_k = [\ \boldsymbol{n}_{\mathrm{N}} \mid \boldsymbol{n}_{\mathrm{T}_x} \mid \boldsymbol{n}_{\mathrm{T}_y}\ ], \tag{3}$$

with $\boldsymbol{n}_{\mathrm{N}}$ denoting the normal vector and $\boldsymbol{n}_{\mathrm{T}_x}$ and $\boldsymbol{n}_{\mathrm{T}_y}$ the in-plane vectors.

Stress–displacement relation. The interaction of particles is governed by constitutive relations that are applied at their contact facets. The mesoscale *elastic* behavior is controlled by two parameters, namely the normal and tangential effective values of elastic interface stiffness E_{N} and E_{T} of the facet k. In elastic regime, the facet stress vector $\boldsymbol{\sigma}$ is a linear transformation

$$\boldsymbol{\sigma}_k = \begin{bmatrix} E_{\mathrm{N}} & & \\ & E_{\mathrm{T}} & \\ & & E_{\mathrm{T}} \end{bmatrix} [\![\boldsymbol{u}_C]\!]_k. \tag{4}$$

In inelastic regime, the contact constitutive behavior comes from the relations described in Section 3, which are formulated at the level of the displacement jump. Let us remark that this contrasts with the original formulation of LDPM [45], introducing effective inter-aggregate strains as $\boldsymbol{\epsilon}_k$ by dividing the displacement jumps with the distance l_{IJ} between the respective particle nodes.

Balance equation. The solution of unknown displacements is obtained via enforcing equilibrium through the Principle of Virtual Work. To this end, we consider the kinematic state $\hat{\boldsymbol{q}}_I^{\mathsf{T}} = [\,\hat{\boldsymbol{u}}_I^{\mathsf{T}} \mid \hat{\boldsymbol{\theta}}_I^{\mathsf{T}}\,]$ of a particle $K = I$ introduced in Eq. (1) together with its energetically conjugated nodal forces $\hat{\boldsymbol{f}}_I$ and moments $\hat{\boldsymbol{m}}_I$ collected in the vector of stress resultants $\hat{\boldsymbol{p}}_I^{\mathsf{T}} = [\,\hat{\boldsymbol{f}}_I^{\mathsf{T}} \mid \hat{\boldsymbol{m}}_I^{\mathsf{T}}\,]$. Then, we equilibrate the work of external resultants $\hat{\boldsymbol{p}}_I$ acting on virtual kinematic nodal values $\delta\hat{\boldsymbol{q}}_J$ with the work of internal forces $A_k\boldsymbol{\sigma}_k$ on virtual displacement jump $\delta[\![\boldsymbol{u}_C]\!]_k$ in a facet k connecting two particles (I, J) to obtain equivalence of global and local virtual work as

$$\delta\hat{\boldsymbol{q}}_J^{\mathsf{T}} \cdot \hat{\boldsymbol{p}}_I = \sum_{k \to (I,J)} \delta[\![\boldsymbol{u}_C]\!]_k^{\mathsf{T}} \cdot A_k\, \boldsymbol{\sigma}_k. \tag{5}$$

The mapping between the facet values indexed by k and nodal values (I, J) is established by expressing the virtual displacement jump $[\![\boldsymbol{u}_C]\!]_k^{\mathsf{T}}$ in terms of the nodal displacement and rotations of the associated particles $(\delta\hat{\boldsymbol{q}}_I, \delta\hat{\boldsymbol{q}}_J)$ in analogy to the real strains $\boldsymbol{\varepsilon}_k$, using Eqs. (3), (2), and (1). Then, a consistent representation of the virtual kinematic variables of Eq. (5) is achieved. Since this equality must hold for arbitrary values of $\delta\hat{\boldsymbol{q}}_J$ we finally obtain the global system of I equilibrium equations

$$\hat{\boldsymbol{p}}_I = \boldsymbol{K}_{IJ}\hat{\boldsymbol{q}}_J. \tag{6}$$

3. Thermodynamic formulation for inter-aggregate degradation behavior

To model concrete fatigue, we employ a thermodynamically consistent constitutive framework detailed in [64]. Within this framework, we derive an interface model that can be embedded either on a generic microplane or directly at inter-aggregate contacts in a lattice discrete particle model. The central hypothesis is that fatigue damage in concrete evolves primarily through cumulative inelastic shear strain at inter-aggregate interfaces [63,64]. This approach has been shown to accurately capture the fatigue behavior of cementitious interfaces [70] and concrete under compressive fatigue loading in cylindrical specimens [44,67,71].

3.1. Free energy potential, state variables and thermodynamic forces

As mentioned above, we consider two material points on adjacent aggregates connected by an interface; see Figs. 2 and 4 a. Their relative displacement $\boldsymbol{u}$ is decomposed into a normal (out-of-plane) component $u_{\mathrm{N}} \equiv u_z$, and an in-plane sliding vector $\boldsymbol{u}_{\mathrm{T}} = \{u_x, u_y\}^{\mathsf{T}}$.

To capture irreversible behavior, we introduce the vector of state variables

$$\boldsymbol{\mathcal{E}} := \left[u_{\mathrm{N}}^{\mathrm{p}},\ \omega_{\mathrm{N}}, \boldsymbol{u}_{\mathrm{T}}^{\mathrm{p}},\ \omega_{\mathrm{T}},\ z_{\mathrm{T}},\ \boldsymbol{\alpha}_{\mathrm{T}}\right], \tag{7}$$

where

- $u_{\mathrm{N}}^{\mathrm{p}}$ and $\boldsymbol{u}_{\mathrm{T}}^{\mathrm{p}}$ are plastic displacements in the normal and tangential directions, respectively.
- ω_{N} and ω_{T} are scalar damage variables (0: intact, 1: fully damaged) for opening and sliding.
- z_{T} and $\boldsymbol{\alpha}_{\mathrm{T}}$ are internal hardening variables governing kinematic or isotropic hardening in the shear direction.

The Helmholtz free energy per unit volume is expressed as the sum of normal (N) and tangential (T) components

$$\rho\psi(\boldsymbol{u}; \boldsymbol{\mathcal{E}}) = \rho\psi_{\mathrm{N}}(u_{\mathrm{N}}, u_{\mathrm{N}}^{\mathrm{p}}, \omega_{\mathrm{N}}) + \rho\psi_{\mathrm{T}}(\boldsymbol{u}_{\mathrm{T}}, \boldsymbol{u}_{\mathrm{T}}^{\mathrm{p}}, \omega_{\mathrm{T}}, z_{\mathrm{T}}, \boldsymbol{\alpha}_{\mathrm{T}}). \tag{8}$$

This split provides a transparent representation of dissipative mechanisms in the normal and tangential directions.

Normal free energy. We define the normal (N) part, associated with interface opening and closing, as

$$\rho\psi_{\mathrm{N}}(u_{\mathrm{N}}, u_{\mathrm{N}}^{\mathrm{p}}, \omega_{\mathrm{N}}) := \frac{1}{2}\left[1 - H(\sigma_N)\omega_{\mathrm{N}}\right] E_{\mathrm{N}}(u_{\mathrm{N}} - u_{\mathrm{N}}^{\mathrm{p}})^2, \tag{9}$$

where E_{N} is the undamaged normal stiffness, σ_N the normal traction, and $H(\cdot)$ the Heaviside function enforcing unilateral damage activation only in tension. Under compression ($\sigma_N < 0$), $H(\sigma_N) = 0$ and the interface remains undamaged. Switching off the damage in compression represents the stiffness recovery upon interface closure.

Tangential free energy. The sliding contribution to the Helmholtz free energy is defined as a function of the total sliding vector $\boldsymbol{u}_{\mathrm{T}}$, plastic sliding vector $\boldsymbol{u}_{\mathrm{T}}^{\mathrm{p}}$, tangential damage ω_{T}, and the displacement variables corresponding to isotropic and kinematic hardening, z_{T} and $\boldsymbol{\alpha}_{\mathrm{T}} = [\alpha_x, \alpha_y]$, respectively, as

$$\rho\psi_{\mathrm{T}}(\boldsymbol{u}_{\mathrm{T}}; \boldsymbol{u}_{\mathrm{T}}^{\mathrm{p}}, \omega_{\mathrm{T}}, z_{\mathrm{T}}, \boldsymbol{\alpha}_{\mathrm{T}}) := \frac{1}{2}\left[1 - \omega_T\right] E_{\mathrm{T}}\left[(\boldsymbol{u}_{\mathrm{T}} - \boldsymbol{u}_{\mathrm{T}}^{\mathrm{p}})^{\mathsf{T}} \cdot (\boldsymbol{u}_{\mathrm{T}} - \boldsymbol{u}_{\mathrm{T}}^{\mathrm{p}})\right] + \frac{1}{2}K z_{\mathrm{T}}^2 + \frac{1}{2}\gamma(\boldsymbol{\alpha}_{\mathrm{T}}{}^{\mathsf{T}} \cdot \boldsymbol{\alpha}_{\mathrm{T}}), \tag{10}$$

where E_{T} denotes the tangential stiffness, K the isotropic and γ the kinematic hardening moduli.

Thermodynamic forces. To distinguish the thermodynamic forces in correspondence with the state vector in Eq. (7), we introduce the generalized vector of thermodynamic forces

$$\boldsymbol{S} := \left[\sigma_{\mathrm{N}}^{\mathrm{p}},\ Y_{\mathrm{N}},\ \boldsymbol{\sigma}_{\mathrm{T}}^{\mathrm{p}},\ Y_{\mathrm{T}},\ Z_{\mathrm{T}},\ \boldsymbol{X}_{\mathrm{T}}\right]. \tag{11}$$

These conjugate forces are obtained by differentiation of ψ with respect to state variables

$$\boldsymbol{S} = \boldsymbol{Y}\ \frac{\partial\,\rho\psi(\boldsymbol{\mathcal{E}})}{\partial\,\boldsymbol{\mathcal{E}}}, \tag{12}$$

where $\boldsymbol{Y} = [-1,\ -1,\ -1,\ -1,\ 1,\ 1]$ is a sign operator distinguishing softening and hardening mechanisms ensuring the sign consistency between conjugate forces and state variables. The normal plastic stress $\sigma_{\mathrm{N}}^{\mathrm{p}}$ and normal energy release rate Y_{N} then read

$$\sigma_{\mathrm{N}}^{\mathrm{p}} = -\rho\frac{\partial\psi(\boldsymbol{\mathcal{E}})}{\partial u_{\mathrm{N}}^{\mathrm{p}}} = \left(1 - H(\sigma_{\mathrm{N}}^{\mathrm{p}})\,\omega_{\mathrm{N}}\right) E_{\mathrm{N}}(u_{\mathrm{N}} - u_{\mathrm{N}}^{\mathrm{p}}), \tag{13}$$

$$Y_{\mathrm{N}} = -\rho\frac{\partial\psi(\boldsymbol{\mathcal{E}})}{\partial\omega_{\mathrm{N}}} = \frac{1}{2}E_{\mathrm{N}}(u_{\mathrm{N}} - u_{\mathrm{N}}^{\mathrm{p}})^2. \tag{14}$$

The tangential plastic stress vector $\boldsymbol{\sigma}_{\mathrm{T}}^{\mathrm{p}}$, energy release rate Y_{T} are obtained analogously as

$$\boldsymbol{\sigma}_{\mathrm{T}}^{\mathrm{p}} = -\rho \frac{\partial \psi(\boldsymbol{\mathcal{E}})}{\partial \boldsymbol{u}_{\mathrm{T}}^{\mathrm{p}}} = (1-\omega_{\mathrm{T}}) E_{\mathrm{T}} (\boldsymbol{u}_{\mathrm{T}} - \boldsymbol{u}_{\mathrm{T}}^{\mathrm{p}}), \tag{15}$$

$$Y_{\mathrm{T}} = -\rho \frac{\partial \psi(\boldsymbol{\mathcal{E}})}{\partial \omega_{\mathrm{T}}} = \frac{1}{2} E_{\mathrm{T}} \left[(\boldsymbol{u}_{\mathrm{T}} - \boldsymbol{u}_{\mathrm{T}}^{\mathrm{p}})^{\mathsf{T}} \cdot (\boldsymbol{u}_{\mathrm{T}} - \boldsymbol{u}_{\mathrm{T}}^{\mathrm{p}}) \right]. \tag{16}$$

The forces conjugate to z_{T} and $\boldsymbol{\alpha}_{\mathrm{T}}$ define the isotropic hardening stress Z_{T} and the back stress $\boldsymbol{X}_{\mathrm{T}} = \{X_x, X_y\}^{\mathsf{T}}$, respectively, defined as:

$$Z_{\mathrm{T}} = \rho \frac{\partial \psi(\boldsymbol{\mathcal{E}})}{\partial z_{\mathrm{T}}} = K z_{\mathrm{T}}, \tag{17}$$

$$\boldsymbol{X}_{\mathrm{T}} = \rho \frac{\partial \psi(\boldsymbol{\mathcal{E}})}{\partial \boldsymbol{\alpha}_{\mathrm{T}}} = \gamma\, \boldsymbol{\alpha}_{\mathrm{T}}. \tag{18}$$

This completes the definition of conjugate forces, setting the stage for yield criteria, flow rules, and damage evolution laws under a unified thermodynamic framework.

3.2. Threshold function

The threshold function defines the elastic domain in terms of effective normal and tangential stresses, $\tilde{\sigma}_{\mathrm{N}}$ and $\tilde{\boldsymbol{\sigma}}_{\mathrm{T}}$, characterizing the undamaged skeleton. These relate to their apparent counterparts via

$$\tilde{\sigma}_{\mathrm{N}} = \frac{\sigma_{\mathrm{N}}^{\mathrm{p}}}{1 - H(\sigma_{\mathrm{N}}^{\mathrm{p}})\omega_{\mathrm{N}}} = E_{\mathrm{N}}(u_{\mathrm{N}} - u_{\mathrm{N}}^{\mathrm{p}}), \tag{19}$$

$$\tilde{\boldsymbol{\sigma}}_{\mathrm{T}} = \frac{\boldsymbol{\sigma}_{\mathrm{T}}^{\mathrm{p}}}{1-\omega_{\mathrm{T}}} \qquad = E_{\mathrm{T}}(\boldsymbol{u}_{\mathrm{T}} - \boldsymbol{u}_{\mathrm{T}}^{\mathrm{p}}). \tag{20}$$

The shape of the elastic domain in effective stress space is illustrated in Fig. 4(b). The shear threshold function follows an enhanced Mohr–Coulomb criterion

$$f_{\mathrm{T}} = \tilde{q}_{\mathrm{T}} - (f_{\mathrm{cs}} + Z_{\mathrm{T}}) + m\,\tilde{\sigma}_{\mathrm{N}}, \tag{21}$$

where a stress-like norm $\tilde{q}_{\mathrm{T}} = \|\tilde{\boldsymbol{\sigma}}_{\mathrm{T}} - \boldsymbol{X}_{\mathrm{T}}\|$ captures tangential behavior relative to the back stress $\boldsymbol{X}_{\mathrm{T}}$ and f_{cs} is the shear strength limit and m controls pressure sensitivity. This form is suitable for shear-dominated problems like pull-out tests [63], but insufficient when normal and tangential dissipation mechanisms interact.

To model interactions between normal and tangential dissipation, we employ a smooth multi-domain level-set envelope with tension, compression, and shear subdomains.

The tensile and compressive domains are modeled with ellipses, $f_{\mathrm{N}}^{\mathrm{t}}$ and $f_{\mathrm{N}}^{\mathrm{c}}$, and smoothly transition into the shear domain f_{T}, as shown in Fig. 3b. The linear and elliptic parts oof the threshold function are expressed as

$$f_{\mathrm{lin}}(x, y; \bar{y}, x_0, m) = |y| - \bar{y} + m(x - x_0), \tag{22}$$

$$f_{\mathrm{ell}}(x, y; \bar{x}, \bar{y}, x_0, m) = \sqrt{\frac{y^2}{b^2} + \frac{(x - x_0 - x_{\mathrm{c}})^2}{a^2}} - c. \tag{23}$$

The parameters a, b, c, and x_c are derived in a closed form in [64] using the continuity and smoothness conditions, that are summarized in Fig. 3a; here we provide the resulting expressions (with $\hat{x} = x_0 - \bar{x}$)

$$c = \bar{y} + \frac{m^2 \hat{x}^2}{2m\hat{x} + \bar{y}}, \qquad a = -\frac{\bar{y} - m\hat{x}}{\bar{y} - 2m\hat{x}} \cdot \frac{\hat{x}}{c}, \qquad b = \frac{\bar{y} - m\hat{x}}{\sqrt{\bar{y} - 2\,m\hat{x}}} \cdot \frac{\sqrt{\bar{y}}}{c}, \qquad x_c = -\frac{m\hat{x}^2}{2m\hat{x} + \bar{y}}. \tag{24}$$

Substituting these expressions into Eqs. (22) and (23) yields the complete smooth threshold function with explicitly defined gradients w.r.t. thermodynamic forces. The tensile and compressive regimes can be instantiated by the substitutions

$$\mathcal{N}^{\mathrm{t}} := \{x = \tilde{\sigma}_{\mathrm{N}}, y = \tilde{q}_{\mathrm{T}}, \bar{x} = f_{\mathrm{ct}}, \bar{y} = f_{\mathrm{cs}} + Z, x_0 = 0\}, \tag{25}$$

$$\mathcal{N}^{\mathrm{c}} := \{x = -\tilde{\sigma}_{\mathrm{N}}, y = \tilde{q}_{\mathrm{T}}, \bar{x} = f_{\mathrm{cc}}, \bar{y} = f_{\mathrm{cs}} + Z, x_0 = f_{\mathrm{c0}}\}. \tag{26}$$

This formulation ensures a smooth transition between normal and tangential mechanisms under various loading conditions, as illustrated in Fig. 3.

3.3. Non-associative flow potential accounting for damage interaction

The flow potential extends the yield function $f(\boldsymbol{\mathcal{E}}, \boldsymbol{S})$ by incorporating damage evolution in normal and shear directions, ω_{N} and ω_{T}. Following [64], the essential mechanism capturing fatigue degradation is plastic sliding–driven damage combined with kinematic hardening.

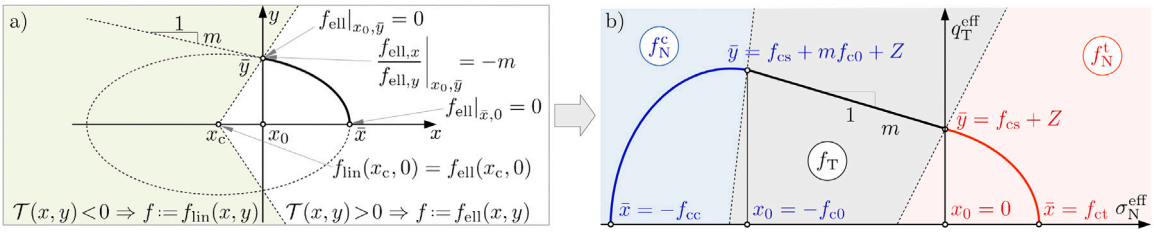


Fig. 3. Construction of a continuous and smooth transition between elliptical and linear parts of the threshold function.

During a loading cycle, tangential deformations within the elastic range do not contribute to damage. Once the deformation surpasses the yield threshold, plastic flow initiates, driving damage growth and shifting the elastic domain through kinematic hardening. Upon unloading, a reverse domain shift is needed to cause a further damage—a critical feature for modeling cyclic fatigue. Without the damage propagation during unloading phase, the model would not be relevant for fatigue degradation.

Normal–tangential coupling in damage evolution is introduced via a scalable mechanism governed by the parameter $\eta \in \langle 0, 1 \rangle$. This approach, proposed in [64], enables a smooth transition between uncoupled ($\eta = 0$) and fully coupled ($\eta = 1$) damage growth:

$$\varphi(\boldsymbol{\mathcal{E}}, \boldsymbol{\mathcal{S}}) := f(\boldsymbol{\mathcal{E}}, \boldsymbol{\mathcal{S}}) + (1-\eta)\left(\varphi_{\text{N}} + \varphi_{\text{T}}\right) + \eta\, \varphi_{\text{NT}} \tag{27}$$

where

- φ_{N} and φ_{T} are pure-mode flow potentials in normal and tangential directions, respectively.
- φ_{NT} is a combined-mode flow potential capturing interaction between opening and sliding damages.

This non-associative form ensures that the plastic flow direction and damage evolution reflect the mixed-mode interaction prescribed by η, providing flexibility to calibrate coupling effects against experimental fatigue data. The pure-mode potentials φ_{N} and φ_{T} depend on the corresponding amounts of stored energies Y_{N} and Y_{T}

$$\varphi_{\text{N}} := (1-\omega_{\text{N}})^{c_{\text{N}}} \frac{S_{\text{N}}}{r_{\text{N}}+1}\left(\frac{Y_{\text{N}}}{S_{\text{N}}}\right)^{r_{\text{N}}+1} H(\sigma_{\text{N}}^{\text{p}}), \qquad \varphi_{\text{T}} := (1-\omega_{\text{T}})^{c_{\text{T}}} \frac{S_{\text{T}}}{r_{\text{T}}+1}\left(\frac{Y_{\text{T}}}{S_{\text{T}}}\right)^{r_{\text{T}}+1} \tag{28}$$

The fully coupled potential φ_{NT}

$$\varphi_{\text{NT}} := (1-\omega_{\text{NT}})^{c_{\text{NT}}} \frac{S_{\text{NT}}}{r_{\text{NT}}+1}\left(\frac{Y_{\text{N}}+Y_{\text{T}}}{S_{\text{NT}}}\right)^{r_{\text{NT}}+1} \tag{29}$$

uses the geometric averages of the material parameters

$$S_{\text{NT}} := \sqrt{S_{\text{N}} S_{\text{T}}}, \quad c_{\text{NT}} := \sqrt{c_{\text{N}} c_{\text{T}}}, \quad r_{\text{NT}} := \sqrt{r_{\text{N}} r_{\text{T}}} \tag{30}$$

The coupled damage variable ω_{NT} is defined as the geometric mean of the integrity variables

$$1 - \omega_{\text{NT}} := \sqrt{(1-\omega_{\text{N}})(1-\omega_{\text{T}})} \tag{31}$$

This ensures a consistent interpolation: for small values of damage, $\omega_{\text{NT}} \approx (\omega_{\text{N}} + \omega_{\text{T}})/2$, while for large values, it approaches $\max(\omega_{\text{N}}, \omega_{\text{T}})$.

3.4. Evolution equations

The flow direction is defined as the product of the sign operator Y and the gradient of the flow potential with respect to the state variables. This yields the flow direction vector:

$$\boldsymbol{\Phi}(\boldsymbol{\mathcal{E}}, \boldsymbol{\mathcal{S}}) = -Y \frac{\partial \varphi(\boldsymbol{\mathcal{E}}, \boldsymbol{\mathcal{S}})}{\partial \boldsymbol{\mathcal{S}}} \tag{32}$$

The evolution equations (normality rule) for the state variables then take the form:

$$\dot{\boldsymbol{\mathcal{E}}} = \lambda\, \boldsymbol{\Phi}(\boldsymbol{\mathcal{E}}, \boldsymbol{\mathcal{S}}) = -\lambda\, Y \frac{\partial \varphi(\boldsymbol{\mathcal{E}}, \boldsymbol{\mathcal{S}})}{\partial \boldsymbol{\mathcal{S}}} \tag{33}$$

The summarized inter-aggregate constitutive model, which describes the behavior of interfaces with 3D kinematics under all possible mixed-mode stress configurations during monotonic, cyclic, and fatigue loading, is illustrated in Fig. 4. Compared to state-of-the-art models, the employed interface constitutive model exhibits the following salient features: (i) the evolution equations derived from the potentials are formulated such that damage evolves in conjunction with the cumulative plastic sliding measure, (ii) the convex, continuous, and smooth shape of the threshold function (Fig. 4b), defined in the effective stress domain, enables a robust and efficient time integration scheme that automatically accounts for unloading and reloading, and (iii) the non-associative flow potential incorporates a scalable coupling between normal and tangential damage evolution.

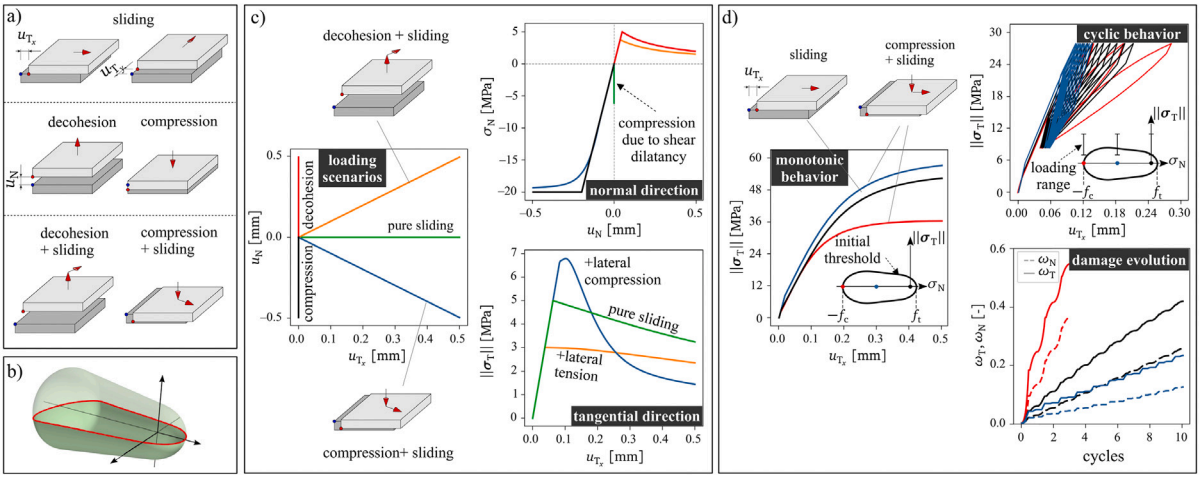


Fig. 4. Inter-aggregate fatigue constitutive model: (a) Kinematic modes; (b) Initial smooth threshold function delineating the elastic domain in stress space; (c) Elementary behavior under proportional monotonic loading; (d) Sensitivity to the lateral compression and cumulative sliding damage under fatigue loading.

The inter-aggregate interface model captures key coupling effects under proportional loading, including pure tension, compression, sliding, and mixed-mode scenarios as shown in Fig. 4c. The response in the normal direction shows that combined normal-tangential loading reduces the tensile or compressive strength compared to pure mode behavior, due to the smooth threshold function that yields peak strength only under pure decohesion or compression. Similarly, the response in the tangential direction demonstrates that shear strength increases under lateral compression and decreases under lateral tension, reflecting trends observed in experimental studies of concrete interfaces [72–75]. Furthermore, the facet interface model effectively captures subcritical cyclic sliding under varying levels of normal confinement in force-controlled fatigue loading. The simulations shown in Fig. 4d reveal a cyclic vertex effect, where moderate confinement delays damage evolution, while high confinement accelerates failure after only a few cycles. This behavior is reflected in the stress–slip curves and damage evolution trends, demonstrating the ability of the model to represent the influence of confinement on fatigue performance, including the evolution of hysteresis loop shapes under cyclic loading. The integration of the evolution equations is conducted using a backward Euler scheme with a Newton iteration loop implementing return mapping and state update steps. The stability and efficiency of the return mapping are achieved through fully resolved gradients of the governing free energy potential in combination with the threshold function, implemented within a symbolic algebra framework. Further details on the model formulation and its response under a wide range of loading conditions are provided in [64].

3.5. Energy breakdown

Energy dissipated within the inter-aggregates regions provides a quantitative measure of irreversible mechanisms such as plastic deformation, plastic hardening, and damage evolution. The possibility to isolate the energy release associated with individual mechanisms enables an objective assessment of their role in stress redistribution and interface degradation under various loading scenarios as described in [64]. The thermodynamic admissibility of the inter-aggregate model under any loading scenario is verified through the Clausius–Duhem inequality ($\mathcal{D} \geq 0$), where the dissipation $\mathcal{D}$ is the sum of normal and tangential contributions:

$$\mathcal{D} = \mathcal{D}_{\mathrm{N}} + \mathcal{D}_{\mathrm{T}} = -\frac{\partial \rho\psi(\boldsymbol{\mathcal{E}})}{\partial \boldsymbol{\mathcal{E}}} \cdot \dot{\boldsymbol{\mathcal{E}}} = -\left[\frac{\partial \rho\psi_{\mathrm{N}}(\boldsymbol{\mathcal{E}})}{\partial \boldsymbol{\mathcal{E}}} \cdot \dot{\boldsymbol{\mathcal{E}}} + \frac{\partial \rho\psi_{\mathrm{T}}(\boldsymbol{\mathcal{E}})}{\partial \boldsymbol{\mathcal{E}}} \cdot \dot{\boldsymbol{\mathcal{E}}}\right], \tag{34}$$

The normal and tangential components read

$$\mathcal{D}_{\mathrm{N}} = \sigma_{\mathrm{N}}^{p} \dot{u}_{\mathrm{N}}^{p} + Y_{\mathrm{N}} \dot{\omega}_{\mathrm{N}}, \qquad \mathcal{D}_{\mathrm{T}} = \boldsymbol{\sigma}_{\mathrm{T}}^{p} \cdot \dot{\boldsymbol{u}}_{\mathrm{T}}^{p} - (Z_{\mathrm{T}} \dot{z}_{\mathrm{T}} + \boldsymbol{X}_{\mathrm{T}} \cdot \dot{\boldsymbol{\alpha}}_{\mathrm{T}}) + Y_{\mathrm{T}} \dot{\omega}_{\mathrm{T}}, \tag{35}$$

where the first terms represent plastic dissipation and the latter terms correspond to damage dissipation. Plastic dissipation for both directions is

$$\mathcal{D}^{\mathrm{P}} = \sigma_{\mathrm{N}}^{p} \dot{u}_{\mathrm{N}}^{p} + \boldsymbol{\sigma}_{\mathrm{T}}^{p} \cdot \dot{\boldsymbol{u}}_{\mathrm{T}}^{p} - (Z_{\mathrm{T}} \dot{z}_{\mathrm{T}} + \boldsymbol{X}_{\mathrm{T}} \cdot \dot{\boldsymbol{\alpha}}_{\mathrm{T}}) = \mathcal{W}^{\mathrm{P}} - (\mathcal{U}^{\mathrm{iso}} + \mathcal{U}^{\mathrm{kin}}), \tag{36}$$

where $\mathcal{W}^{\mathrm{P}}$ denotes the plastic work and $\mathcal{U}^{\mathrm{iso}}, \mathcal{U}^{\mathrm{kin}}$ are the free energies associated with isotropic and kinematic hardening [76]. Damage dissipation is given by

$$\mathcal{D}^{\omega} = Y_{\mathrm{N}} \dot{\omega}_{\mathrm{N}} + Y_{\mathrm{T}} \dot{\omega}_{\mathrm{T}}. \tag{37}$$

Table 1
Loading scenarios used for the calibration and validation of the developed LDPM model.

Loading scenario		Description	Role for material behavior	Role for structural behavior
LS1		Monotonic loading	Calibration targeting macroscopic Young's modulus E_{mac}, onset of inelasticity σ^{inel}_{mac}, strain at peak ϵ_{mac} and macroscopic strength f_{mac} (Fig. 5a)	Identification of peak load
LS2		Step-wise increased cyclic loading	Calibration targeting the final secant stiffness E_{final} (Fig. 5d)	Validation via comparison with experiment
LS3		Fatigue loading with constant amplitudes	Calibration of S–N curve and Sparks–Menzies relation, targeting the slopes m_{S-N} and m_{S-M} (Fig. 6cd)	Parametric study of fatigue behavior

The total input work decomposes as $\mathcal{W}^{tot} = \mathcal{W}^{el} + \mathcal{W}^{in}$, with $\mathcal{W}^{in} = \mathcal{W}^{P} + D^{\omega}$. In summary, the dissipation can be classified into four contributions: (i) normal plastic, (ii) tangential plastic, (iii) normal damage, and (iv) tangential damage. An illustrative example of these components under monotonic loading is provided in Fig. 5.

In the presented discrete model, the above energies evaluated in individual facets are simply multiplied by the facet areas to obtain their contributions in Joules. Summation over all facets reveals the energies in the whole specimen.

4. Material scale: uniaxial monotonic and fatigue response

4.1. Calibration procedure for compressive fatigue

While cylinder tests are commonly used to characterize concrete fatigue behavior, this study employs rectangular prisms for material model calibration. The prismatic geometry was chosen because it represents a cut-out from the compression zone of the prestressed beam tests analyzed in Section 5. The prism dimensions of 50 mm × 50 mm × 100 mm were selected to match the width of the compression zone while providing sufficient space for the discrete representation of the material structure with aggregate size distribution in the range of 8–16 mm.

It is important to emphasize that no new experiments were conducted to obtain calibration data for this study. Instead, the 13 material parameters were calibrated by requiring the model to reproduce standard macroscopic characteristics for concrete grade C30 that are supported by extensive experimental evidence and reported in codes and the literature. Widely established monotonic response data and fatigue characteristics compiled in the fib Model Code 2010 [77] and related references served as the target values for this parameter identification. The calibration was performed using the sequence of loading scenarios LS1-LS3 described in Table 1. Besides the type of loading scenario, Table 1 also highlights the specific calibration focus on prisms and their subsequent use for validation and parametric studies on prestressed beams in Section 5.

In total, seven features of the compressive response were targeted: five related to the stress–strain response, highlighted in green in Figs. 5ad, and two slopes in Figs. 6cd. For monotonic loading (LS1), the model was required to achieve (i) the initial modulus of elasticity E_{mac} = 30 GPa, (ii) the compressive strength $f_{c,mac}$ = 32 MPa, (iii) the associated strain at the peak stress, and (iv) onset of inelasticity at approximately one third of the compressive strength, all four are indicated in Fig. 5a. For the step-wise increasing scenario (LS2), (v) the secant stiffness of the last cycle was assumed to be approximately 65% of the initial stiffness, as depicted in Fig. 5d, based on experimental results in fatigue tests quantified close to fatigue failure [24,78]. The uniform fatigue loading (LS3) was used to adjust the material parameters such that the known Sparks–Menzies relationship [79] and S-N curve [77] were reproduced. The targeted values of double- and semi-logarithmic slopes shown in Figs. 6c–d, were (vi) m_{S-M} = 1.014 and (vii) m_{S-N} = 15.87. The obtained material parameters are listed in Table 2.

To manage the complexity of the manually performed calibration, the procedure was decomposed into the following steps based on the known effects of individual material parameters on the macroscopic response characteristics:

1. Initial elastic response: Two parameters controlling the initial elastic response, namely the mesoscale elastic stiffnesses E_N and E_T, were calibrated first to reproduce the macroscopic elastic response of concrete. The calibration was performed by reversing the analytical homogenization relations from [45].
   At the macroscopic level, concrete is assumed to behave as a statistically homogeneous and isotropic elastic material characterized by Young's modulus E_{mac} and Poisson's ratio ν. These macroscopic quantities are related to the *strain-based* mesoscale elastic moduli $E_N^{(\epsilon)}$ and $E_T^{(\epsilon)}$ through the ratio $\alpha = E_T^{(\epsilon)}/E_N^{(\epsilon)}$, which, in the limiting case of an infinite number of facets per aggregate, yields [45]

$$E_{mac} \approx \frac{2+3\alpha}{4+\alpha} E_N^{(\epsilon)}, \qquad \nu \approx \frac{1-\alpha}{4+\alpha}. \tag{38}$$

   Given the target macroscopic Poisson's ratio $\nu = 0.163$, the above expression can be inverted to obtain $\alpha = (1-4\nu)/(1+\nu) \approx 0.30$. Substituting this value into the homogenization formula for E_{mac} and using the target Young's modulus E_{mac} = 30 GPa (see Fig.

Table 2
Material model parameters identified for experimental concrete mixture.

Parameter	Definition	Value	Unit
Normal parameters (interface opening/decohesion)			
E_N	Normal elastic interface stiffness	2850	[MPa/mm]
f_t	Elastic tensile stress limit	2.5	[MPa]
f_c	Elastic compressive stress limit	27.5	[MPa]
S_N	Damage energy rate scaling parameter	0.0011	[N/mm]
r_N	Damage rate exponent	1.0	[–]
c_N	Damage accumulation exponent	4.0	[–]
Tangential parameters (interface sliding)			
E_T	Tangential elastic stiffness	855	[MPa/mm]
f_s	Elastic shear stress limit	5.0	[MPa]
S_T	Damage energy rate scaling parameter	0.011	[N/mm]
r_T	Damage rate exponent	4.0	[–]
c_T	Damage accumulation exponent	4.0	[–]
γ	Kinematic hardening modulus	1500	[MPa/mm]
Interaction parameter			
η	Damage interaction parameter	0.65	[–]

5a), the strain-based normal mesoscale modulus is obtained as $E_N^{(\varepsilon)} = E_{mac}\,(4+\alpha)/(2+3\alpha) \approx 44.5$ GPa, while the corresponding tangential modulus follows as $E_T^{(\varepsilon)} = \alpha\, E_N^{(\varepsilon)} \approx 13.4$ GPa.
The strain-based mesoscale moduli are subsequently converted into the *displacement-based* input parameters used in the lattice formulation via

$$E_N = \frac{E_N^{(\varepsilon)}}{l_{IJ}}, \qquad E_T = \frac{E_T^{(\varepsilon)}}{l_{IJ}}. \tag{39}$$

Using the average link length $\bar{l}_{IJ} \approx 15$ mm, the above relations provide initial estimates of the displacement-based elastic parameters $\bar{E}_N = 2,967$ MPa/mm and $\bar{E}_T = 893$ MPa/mm. However, since the asymptotic homogenization result is only approximate and the actual LDPM assembly exhibits finite-size effects, geometric disorder, and a limited number of facets per aggregate, the analytical values are not adopted directly. Therefore, a numerical calibration using an explicitly modeled prismatic specimen targeting the macroscopic Young's modulus was conducted with initial values set to $\bar{E}_N$ and $\bar{E}_T$. The final values are reported in Table 2.

2. Onset of inelasticity: Three elastic limits (f_t, f_c, f_s) were set to trigger observable macroscopic nonlinearity at approximately one third of the compressive strength, with ratios chosen to render a plausible inelastic threshold shape for concrete.
3. Damage interaction: The single interaction parameter (η) controls the extent to which damage in one mode (e.g., mode I opening) influences damage evolution in the other mode (e.g., mode II sliding). The value $\eta = 0.65$ represents moderate coupling [64].

The remaining seven parameters, three for the normal direction (S_N, r_N, c_N), and four for the tangential direction (S_T, r_T, c_T, γ), exhibit strong interactions and were calibrated manually as follows:

4. Shape of the ascending stress–strain curve and the value of unloading stiffness: Damage scaling parameters and kinematic hardening modulus (S_N, S_T, γ) were calibrated to reproduce the peak stress f_{mac} and associated strain ε_{mac} and unloading stiffness E_{final} under uniaxial compression; see Figs. 5ad.
5. Fatigue response: Damage rate exponents (r_N, r_T) and damage accumulation exponents (c_N, c_T) were calibrated using S-N curves and the Sparks–Menzies relation with the goal to reproduce the slopes m_{S-N} and m_{S-M} shown in Fig. 6c and Fig. 6d, respectively.

The obtained material parameters are listed in Table 2. The computational time required for the iterative calibration on a computer with 16 GB of memory and 16 threads was approximately two minutes for the monotonic loading scenario LS1 and about one and a half minutes per cycle for scenarios LS2 and LS3.

Range of validity. Note that the calibrated model parameters in Table 2 are valid specifically for the chosen aggregate size distribution ranging between $8 - 16$ mm. This distribution was also used to predict the fatigue response of the beam in Section 5. If a discretization with different resolution were used (e.g., finer or coarser aggregate sizes), the parameters would have to be recalibrated, as they implicitly account for the stress redistribution and energy dissipation mechanisms that depend on the resolved material structure. For the considered case of compressive fatigue, the size of the dissipative process zone is significantly larger than the size of individual aggregates. Then, the degradation across many parallel load-bearing paths can be considered evenly distributed, making the response less sensitive to discretization refinement compared to tension-dominated fracture where damage localizes through a narrow process zone. Full discretization objectivity, however, would require energy-based regularization—a topic of ongoing research.

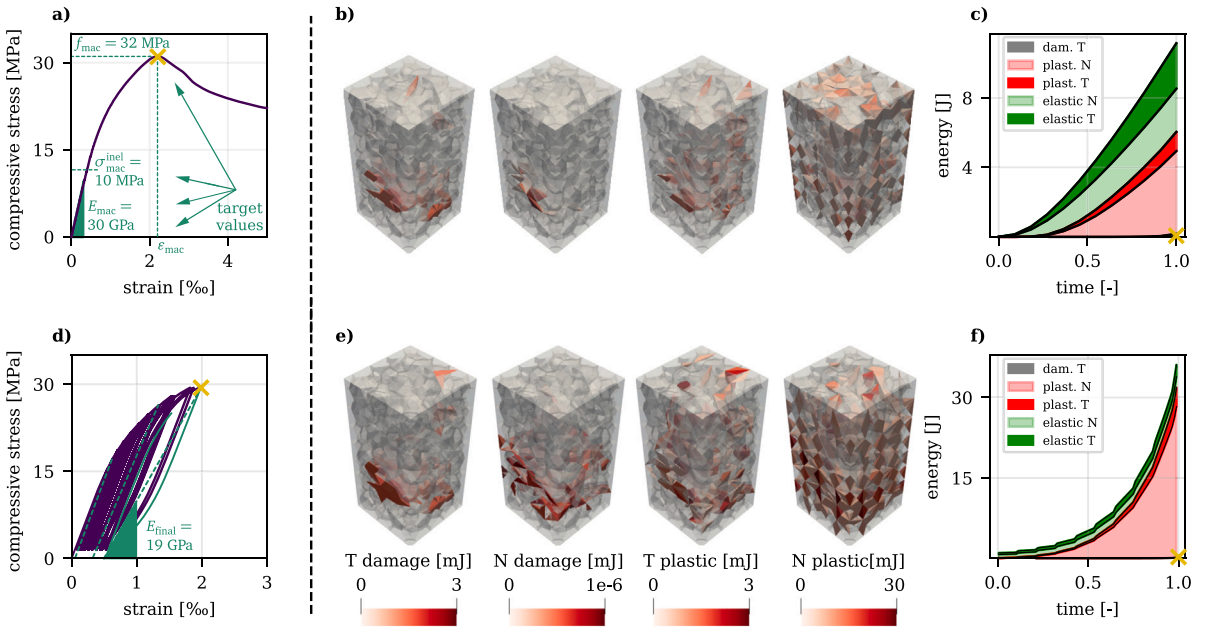


Fig. 5. Energy dissipation in a prismatic specimen subjected to uniaxial compressive loading. Top row (a)–(c): monotonic loading; bottom row (d)–(f): stepwise increasing cyclic loading. (a), (d) Stress–strain response highlighting the selected peak for energy evaluation. (b), (e) Distribution of energy dissipation across the lattice facets at the marked peak, showing contributions from damage (normal and tangential) and plasticity. (c), (f) Integral of dissipated energy with a breakdown of stored and dissipated energy at the marked peak of the stress–strain curve.

4.2. Interpretation of the simulated material response

Monotonic behavior. The uniaxial monotonic response of the calibrated prism is presented in Fig. 5a, showing a peak compressive strength of 32 MPa and an E-modulus of 30 GPa. While the post-peak behavior exhibits high stress levels in the softening regime, the calibrated parameters adequately capture the relevant range of compressive fatigue response. Given the primary focus on fatigue development at subcritical load levels, the calibration is considered acceptable for subsequent studies of fatigue in the pre-peak regime. Fig. 5b illustrates the spatial distribution of energy dissipation due to damage and plasticity at individual facets in the normal and tangential directions evaluated according to Section 3.5. The imposed boundary conditions, which restrict lateral expansion at the top and bottom of the prism, lead to localization near the mid-height of the specimen. Comparison of the maximum values reveals that tangential damage dissipation dominates over normal damage dissipation by several orders of magnitude. Conversely, plastic dissipation in the normal direction significantly exceeds the tangential frictional contribution. The evolution of energy dissipation is further analyzed in Fig. 5c, which plots the breakdown of stored and dissipated energy components over the relative lifetime, ranging from zero to one. The peak load, marked by the yellow cross in Fig. 5a, corresponds to the end of the relative lifetime. Plasticity remains the dominant overall dissipation mechanism, while damage contributions remain negligible.

Step-wise increasing cyclic loading. The simulation results for loading scenario LS2 are presented in the bottom row of Fig. 5. The upper load level begins at $S_{max} = 0.5$, while the lower load level remains constant at $S_{min} = 0.05$. Every ten cycles, the upper load level is incremented by $\Delta S_{max} = 0.05$. The resulting stress–strain response, shown in Fig. 5d, demonstrates the progressive widening of hysteretic loops as the loading approaches the ultimate state, confirming the model's ability to capture damage accumulation during unloading discussed in Section 3.3. Fig. 5e illustrates the spatial distribution of normal and tangential damage, along with plastic dissipation. Compared to monotonic loading, the dissipation patterns under cyclic loading are more uniformly distributed, reflecting a redistribution of inter-aggregate stresses. The energy breakdown over the relative lifetime is plotted in Fig. 5f, from the start of loading to failure, marked by the yellow cross in Fig. 5d. Similar to monotonic loading, plasticity dominates the energy dissipation, while damage contributions remain negligible. However, cyclic loading results in significantly higher overall plastic dissipation.

Uniform fatigue loading. To investigate the effect of fatigue loading, numerical simulations were conducted for loading scenario LS3 with maximum load levels $S_{max} \in [0.800, 0.975]$ in increments of 0.025, while the minimum stress level was held constant at $S_{min} = 0.05$, consistent with the stepwise increasing cyclic loading scenario LS2. The resulting stress–strain and fatigue creep curves are presented in Fig. 6a and Fig. 6b, respectively. The simulated S-N curve, shown in Fig. 6d, is compared to the reference S-N curve for concrete as defined in the Model Code 2010. The model reproduces the overall trend well, particularly at intermediate and high stress levels. However, at lower values of S_{max}, the simulation predicts shorter fatigue life compared to Model Code. Despite this deviation, the reproduced behavior enables meaningful comparisons between the mesoscopic resolution of fatigue degradation

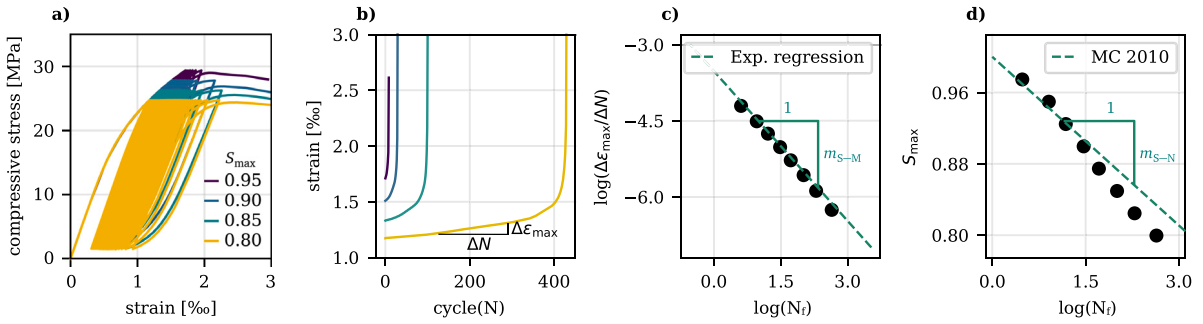


Fig. 6. Simulated uniaxial compressive fatigue behavior under constant-amplitude loading. (a) Stress–strain response over the fatigue life. (b) Fatigue creep curves illustrating strain accumulation with cycle count. (c) Simulated Sparks–Menzies relation: strain rate during the second phase of the fatigue life plotted against number of cycles to failure, compared with the experimental regression from Eq. (6.6) in [79]. (d) Predicted fatigue life from simulations compared to the reference S–N curve for concrete defined in the Model Code 2010 [77].

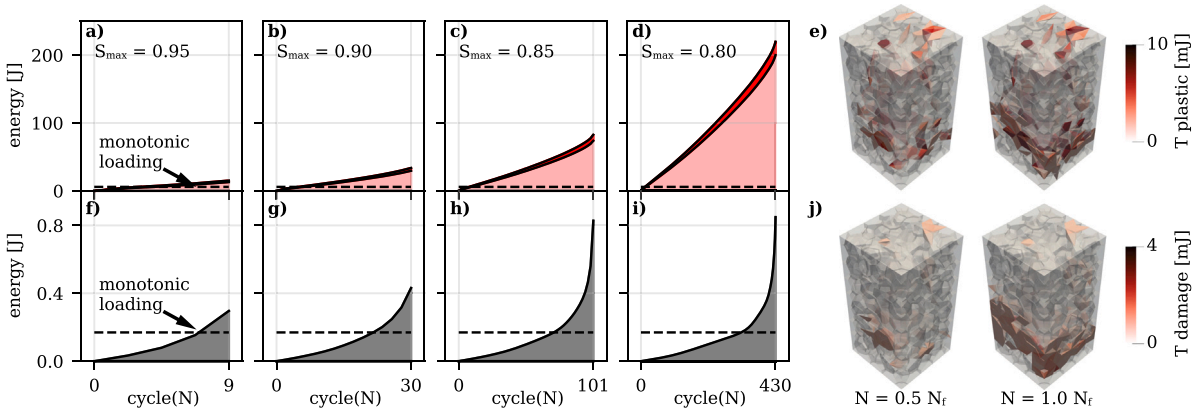


Fig. 7. Breakdown of energy dissipation in each fatigue simulation compared to the reference monotonic loading case (dashed line). (a)–(d) Evolution of plastic dissipation over the number of cycles for the conducted simulations. (e) Spatial distribution of plastic dissipation across lattice facets at failure. Second row: (f)–(i) evolution of damage dissipation over the number of cycles. (j) Spatial distribution of damage dissipation (normal and tangential) at failure.

processes at the material and structural levels. In addition to the S-N curves, the Sparks–Menzies relation was evaluated, as shown in Fig. 6c. This relation captures the correspondence between the rate of fatigue creep during Phase II (highlighted by the yellow curve in Fig. 6b) and the number of cycles-to-failure. The simulated values align well with the experimentally observed trend reported in [79], confirming the ability of the model to capture this critical fatigue characteristic. Energy dissipation is reported in Fig. 7. The top row shows the evolution of plastic energy dissipation over the number of cycles, while the bottom row presents the corresponding damage dissipation. The dashed horizontal line in both rows indicates the corresponding type of energy dissipation observed under monotonic loading up to the peak load. Distinct trends were observed for each dissipative mechanism. Damage dissipation remains approximately constant across all values of S_{max}, suggesting that it is an intrinsic material property independent of the fatigue load range. In contrast, plastic energy dissipation increases with the number of cycles-to-failure due to the cumulative nature of plastic sliding during fatigue loading.

4.3. Role of individual model parameters

To ensure an efficient calibration strategy, it is essential to understand how individual material parameters influence the fatigue response. This understanding provides the necessary foundation for physically meaningful parameter adjustments that target the appropriate aspects of the material behavior during the calibration process.

A parametric study was therefore conducted to evaluate the role of specific material parameters in governing the macroscopic fatigue behavior. The study investigates the influence of the kinematic hardening modulus γ and the damage accumulation parameters c and r on the fatigue response of the material under uniaxial compressive fatigue loading, with results presented in Figs. 8, 9, and 10.

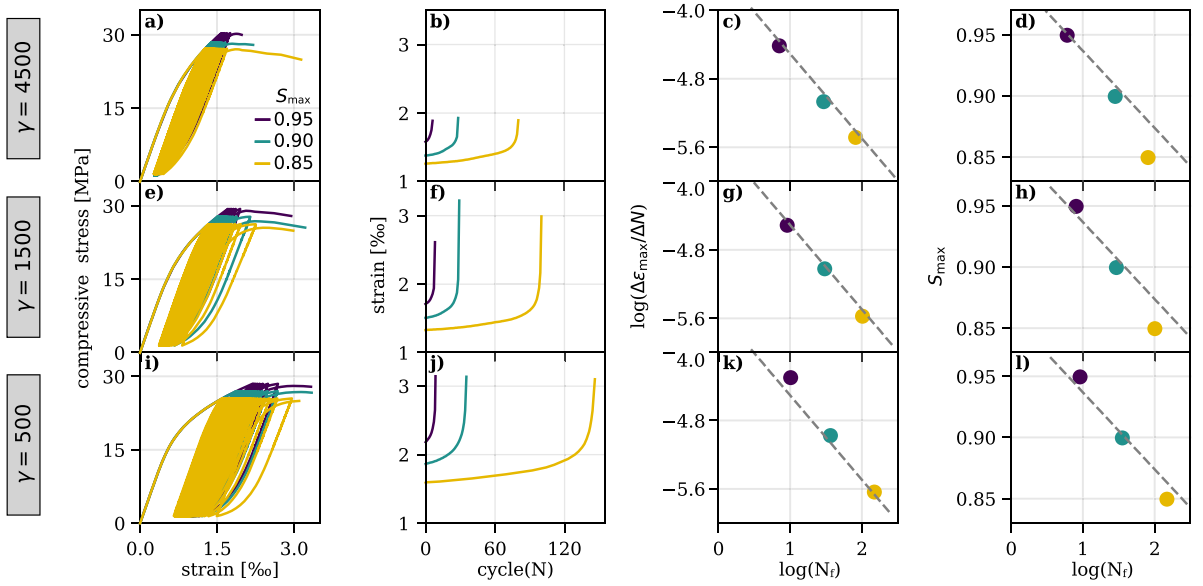


Fig. 8. Influence of the kinematic hardening modulus γ on the uniaxial compressive fatigue behavior under constant amplitude loading. Results are shown for values $\gamma = 500, 1500, 4500$ MPa (from top to bottom). (a), (e), (i) Stress–strain curves under cyclic loading for $S_{max} = 0.85, 0.90, 0.95$; (b), (f), (j) Corresponding creep-fatigue strain evolution over cycles; (c), (g), (k) Simulated Sparks–Menzies relation compared to regression based on experimental campaign – Eq. (6.6) in [79]; (d), (h), (l) Simulated fatigue life compared to the reference S–N curve for concrete defined in the Model Code 2010 [77].

Kinematic hardening modulus γ. The influence of the kinematic hardening modulus γ on the macroscopic fatigue behavior is illustrated in Fig. 8. In this study, the kinematic hardening value was set equal to the specified values shown in the figure, while all the other model parameters were kept constant as listed in Table 2. Increasing γ leads to a noticeable reduction in the width of the hysteresis loops observed in the stress–strain curves (Figs. 8a, e, i), indicating reduced plastic strain accumulation per cycle and a stiffer response. This is further confirmed by the creep-fatigue curves (Figs. 8b, f, j), which show a slower strain accumulation over the number of cycles for higher values of γ.

This increased plastic strain rate translates into a horizontal shift in the Sparks–Menzies relation (Figs. 8c, g, k), with lower γ values resulting in points that lie further to the right, indicating a larger accumulation of plastic deformation per cycle at a given fatigue life. A similar trend is observed in the S–N curves (Figs. 8d, h, l), where reduced hardening slightly increases the number of cycles to failure for a given stress amplitude.

Overall, while the influence of γ on the fatigue life is relatively limited compared to damage-fatigue parameters, it does affect the cyclic plastic response and affects the cumulative deformation under subcritical loading.

Damage accumulation parameter c. The effect of the damage accumulation parameter c on the macroscopic fatigue behavior is illustrated in Fig. 9. In this study, both the normal and tangential damage accumulation parameters were set equal to the specified value of c, while all other model parameters were kept constant as listed in Table 2. This parameter governs the rate at which damage accumulates during cyclic loading and thus directly influences fatigue life.

The stress–strain and creep–fatigue curves (Figs. 9a, e, i) reveal that although variations in exponent c have little impact on the peak load and first ascending branch, they significantly affect the rate of damage evolution, as demonstrated by the changes in fatigue life displayed in Figs. 9b, f, j. This highlights the central role of c in controlling fatigue degradation.

As shown in the Sparks–Menzies plots (Figs. 9c, g, k), a value of c equal to four provides the best agreement with the simulated accumulation of strain per cycle and the experimental trend, indicating a more realistic representation of damage accumulation under subcritical cyclic loading. This effect is also reflected in the S–N curves (Figs. 9d, h, l), where higher values of c lead to longer predicted fatigue lifetimes. The observed trend underscores the critical role of the damage accumulation law in accurately capturing fatigue compressive behavior.

Damage accumulation parameter r. Fig. 10 highlights the influence of the damage accumulation exponent r. In this study, both the normal and tangential damage accumulation parameters were set equal to the specified value of r, while all other model parameters were kept constant as listed in Table 2. This parameter plays a dual role by affecting both the rate of damage accumulation and thus the strength of the material, and the overall fatigue strength of the material. Lower values of r result in a steeper increase in damage per cycle, leading to shorter fatigue lives and at the same time to a higher material strength. As r increases, the material exhibits a more gradual accumulation of damage, significantly extending fatigue life and shifting the Sparks–Menzies relation and the S–N curves to the right (Figs. 9c, g, k and 9d, h, l). In contrast to parameter c, which primarily influences the rate of damage

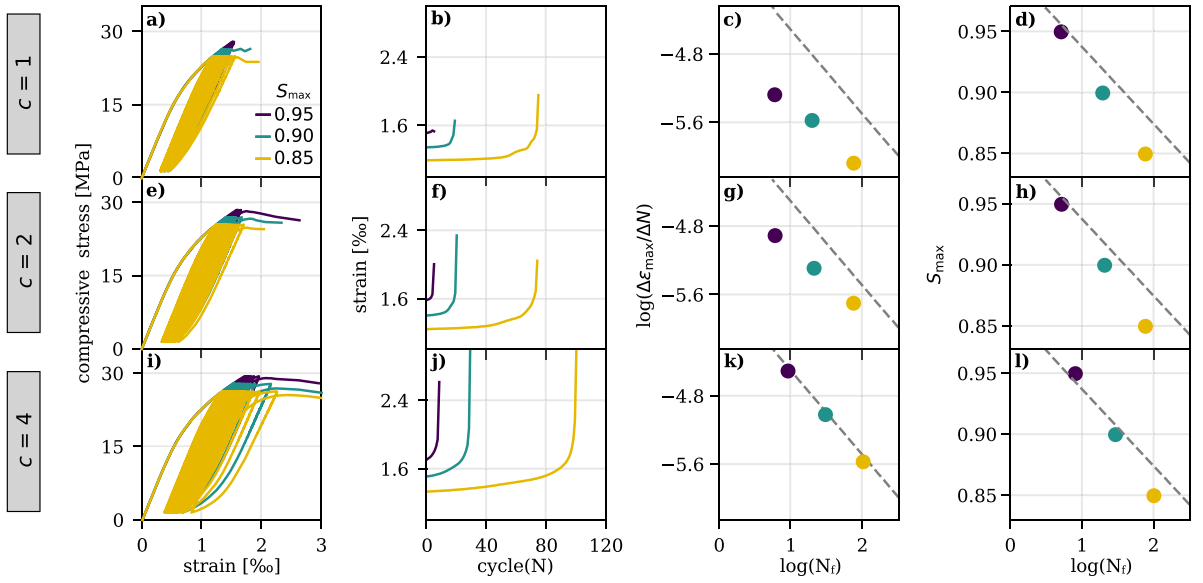


Fig. 9. Influence of the damage parameter c on the uniaxial compressive fatigue behavior under constant amplitude loading. Results are shown for values of $c = 1, 2, 4$ (from top to bottom). (a), (e), (i) Stress–strain curves under cyclic loading for $S_{max} = 0.85, 0.90, 0.95$; (b), (f), (j) Corresponding creep-fatigue strain evolution over cycles; (c), (g), (k) Simulated Sparks–Menzies relation compared to regression based on experimental campaign – Eq. (6.6) in [79]; (d), (h), (l) Simulated fatigue life compared to the reference S–N curve for concrete, compared to Model Code 2010.

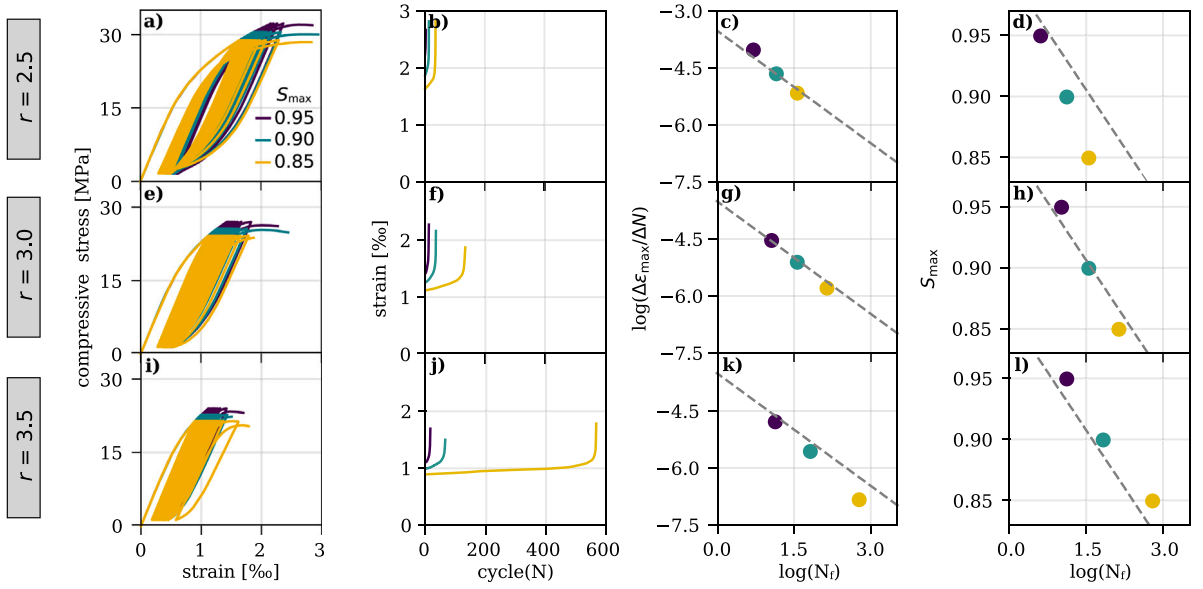


Fig. 10. Influence of the damage parameter r on the uniaxial compressive fatigue behavior under constant amplitude loading. Results are shown for values of $r = 2.5, 3, 3.5$ (from top to bottom). (a), (e), (i) Stress–strain curves under cyclic loading for $S_{max} = 0.85, 0.90, 0.95$; (b), (f), (j) Corresponding creep-fatigue strain evolution over cycles; (c), (g), (k) Simulated Sparks–Menzies relation compared to regression based on experimental campaign – Eq. (6.6) in [79]; (d), (h), (l) Simulated fatigue life compared to the reference S–N curve for concrete, compared to Model Code 2010.

evolution, and controls the horizontal shift of the S-N curve, the parameter r significantly changes both fatigue resistance and material strength. While increasing c slows down the damage accumulation process, it does not substantially affect the macroscopic monotonic peak load. On the other hand, changes in r directly impact the stress response and the fatigue life of the material, specifically by changing the slope of the S-N curve, making it a critical parameter for both accurate fatigue life prediction and capturing the material's mechanical degradation under monotonic loading.

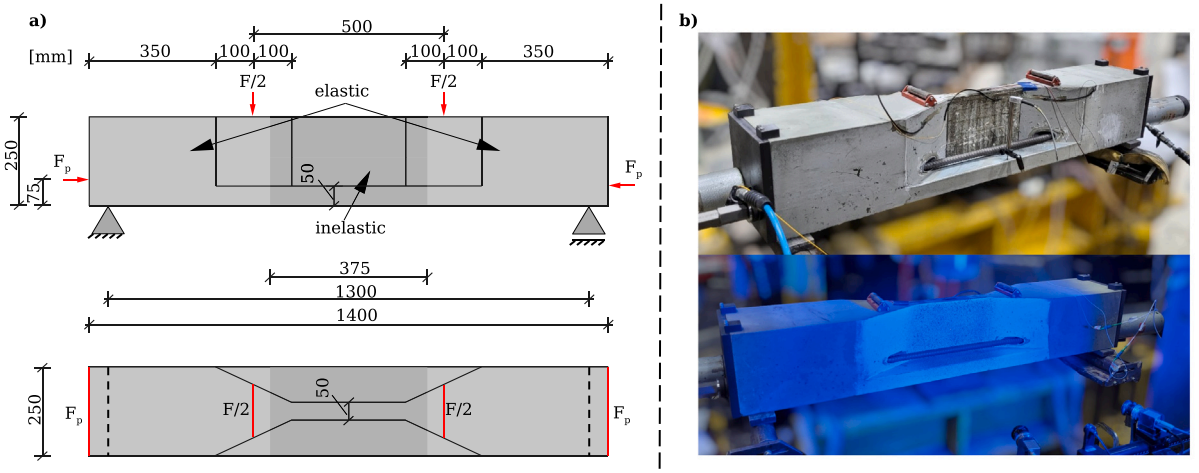


Fig. 11. (a) Proposed geometry for a prestressed four-point bending test of a concrete beam. The schematic illustrates the application points for vertical forces (F/2) and horizontal prestressing forces (F_p). Labels indicating "elastic" and "inelastic" refer to the materials used in simulations. Dimensions are provided in millimeters. (b) Photographic images of the concrete beam during testing, showing the experimental setup with sensors and instrumentation attached to measure structural responses under load.

5. Structural scale: model validation for propagating fatigue

The material parameters previously calibrated using standard uniaxial compressive tests — under both monotonic and fatigue loading conditions — are now employed to reproduce the fatigue behavior of a concrete structural element: an axially prestressed beam subjected to four-point bending. This test configuration has been chosen to introduce spatially non-uniform field in a tested zone possessing a sufficient stress-redistribution capacity.

5.1. Test setup and numerical model

Geometry and boundary conditions. The shape of the prestressed beam was designed to activate the fatigue propagation in the compressive zone between the load points. Therefore, as shown in Fig. 11a, its shape varied along the beam axis from a full section with the width of 25 cm to an inverted T-section with the width of 5 cm. The supports were located 10 cm away from the edges, and the prestressing bars were placed 7.5 cm above the bottom of the beam. The vertical forces F/2 were applied symmetrically, 45 cm away from the edges of the beam.

Recorded data and their processing. As indicated in Fig. 11b, the measured values included the strain field captured using fiber optic sensor (FOS) arranged as grid on the front side of the monitored compression zone, and the displacement field captured using the digital image correlation (DIC) on the back side. Additionally, linear variable differential transformers (LVDTs) complemented these measurement systems by monitoring displacement at selected positions. These data were processed to obtain time-synchronized strain fields in the whole tested zone to construct highly resolved time-space strain functions for a comprehensive model validation.

Loading scenarios. In order to effectively cover the relevant range of fatigue exposures of the material and of the structure, three loading scenarios summarized in Table 1, were applied for the vertical loading of the beam, in analogy to the numerical tests on prisms described in Section 4. Prior to the vertical loading a constant horizontal prestressing force $F_p = 400$ kN was applied, see Fig. 11a. To avoid rate-dependent effects on the fatigue degradation, the frequency of fatigue loading was set as low as 1 Hz. As shown on experimental results in [14], at this low frequency, the effect of the loading rate on the fatigue response remains negligible. This justifies the usage of the rate-independent constitutive model summarized in Section 3 for the analysis of the fatigue behavior.

Evaluated fatigue characteristics. The obtained response has been transformed into quantitative characteristics of the fatigue degradation process, namely S-N and Spark-Menzies curves, which link the tested fatigue load levels and the monitored rates of fatigue creep curves to the numbers of cycles to failure, respectively. These characteristics allow us to set the obtained results into a broader context of concrete fatigue characterization.

Numerical model setup. To ensure symmetric application of loads and constraints, nodes were evenly distributed across the beam width at the corresponding locations. To reduce the computational cost of the mesoscale discrete model, the outer regions, where no significant inelastic phenomena were expected, were modeled using an elastic material with a coarser aggregate size. These regions are indicated in Fig. 11a by light and dark gray shading. In the elastic zones, the minimum and maximum aggregate sizes were set to 16 mm and 32 mm, respectively, while in the inelastic core, they ranged from 8 mm to 16 mm. A prestressing force of 400 kN, consistent with the experimental setup, was applied at the beginning of each simulation and maintained constant throughout. The

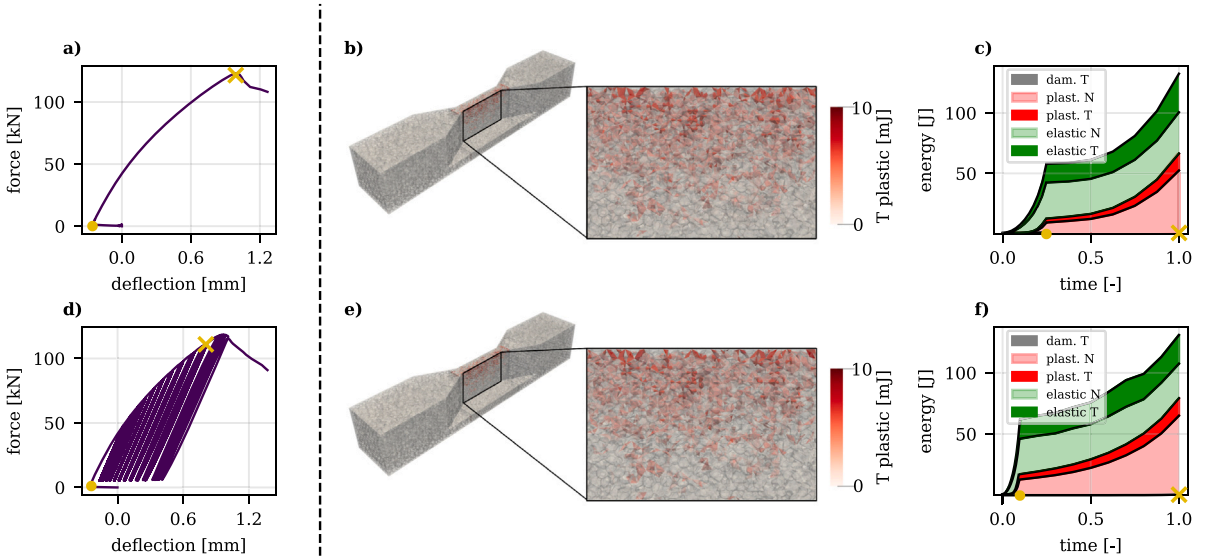


Fig. 12. Energy dissipation in the prestressed bending test under bending action. Top row (a)–(c): monotonic loading; bottom row (d)–(f): stepwise increasing cyclic loading. (a), (d) Stress–strain response highlighting the selected peak for energy evaluation. (b), (e) Distribution of energy dissipation across the lattice facets at the marked peak, showing contributions from damage (normal and tangential) and plasticity. (c), (f) Integral of dissipated energy with a breakdown of stored and dissipated energy at the marked peak of the stress–strain curve.

material parameters used in the inelastic region were calibrated based on prism tests. With the chosen resolution of the material structure, the calculation time for a single cycle was 26 min, using parallelized code on an Intel Xeon 50-core processor.

5.2. Monotonic behavior

The loading scenario LS1 in Table 1 was applied numerically with the parameters obtained using the prisms and summarized in Table 2. The obtained response shown in Fig. 13 reproduced the peak load that was close to the value obtained during the preliminary dimensioning of the setup. A good prediction of the peak was further confirmed by the tests loaded with the stepwise increasing loading scenario LS2 shown in Fig. 13. The obtained ultimate vertical force $F = 123$ kN was therefore used as the reference load for the subsequent fatigue loading ranges $S_{\max}, S_{\min}$.

As illustrated in Fig. 12a, the force–deflection calculated using the calibrated model, including the prestressing and loading phases delivers the expected peak vertical force of approximately 123 kN with a corresponding mid-span deflection of 0.8 mm. The beam demonstrates a distinctive nonlinear response, characterized by a progressive reduction of stiffness before reaching the peak load.

The degradation of the material is visualized through the spatial distribution of plastic energy dissipation at the peak load, as shown in Fig. 12b. The results indicate an evenly distributed degradation within the compression zone in the upper region of the beam. Compared to the prisms shown in Fig. 5, the energy dissipation pattern in the beam appears less localized. This observation suggests a higher degree of parallel bond activation within the aggregate system, facilitating a more uniform degradation process during stress redistribution in the compressive zone. This aspect is particularly relevant for the interpretation of fatigue-induced stress redistribution, which is explored in the subsequent sections.

The energy breakdown (Fig. 12c) illustrates the evolution of stored elastic energy alongside plastic and damage-induced dissipation. It is worth noting that the stored energy increases during prestressing and remains nearly constant for a subsequent monotonically increasing vertical load. This is plausible when we realize that the flexural loading increases the strain at the top and decreases it at the bottom of the beam. At the peak load, elastic storage reaches approximately 52 J. The major fraction of energy dissipation, around 66 J, is attributed to plastic deformation in both normal and tangential directions. In contrast, the contribution of damage-induced dissipation is minimal, approximately 0.4 J. This indicates that the primary dissipative mechanism under monotonic loading are plastic compressive crushing and tangential sliding within the cement paste. This observation is consistent with the results obtained on monotonically loaded prisms.

5.3. Step-wise increasing cyclic loading

In analogy to the simulation of prisms, the loading scenario LS2 from Table 1 started at $S_{\max} = 0.40$ corresponding to an applied vertical force of $F = 49$ kN and was incrementally increased by $\Delta S = 0.05$, i.e. 7 kN, after performing a prescribed number of cycles.

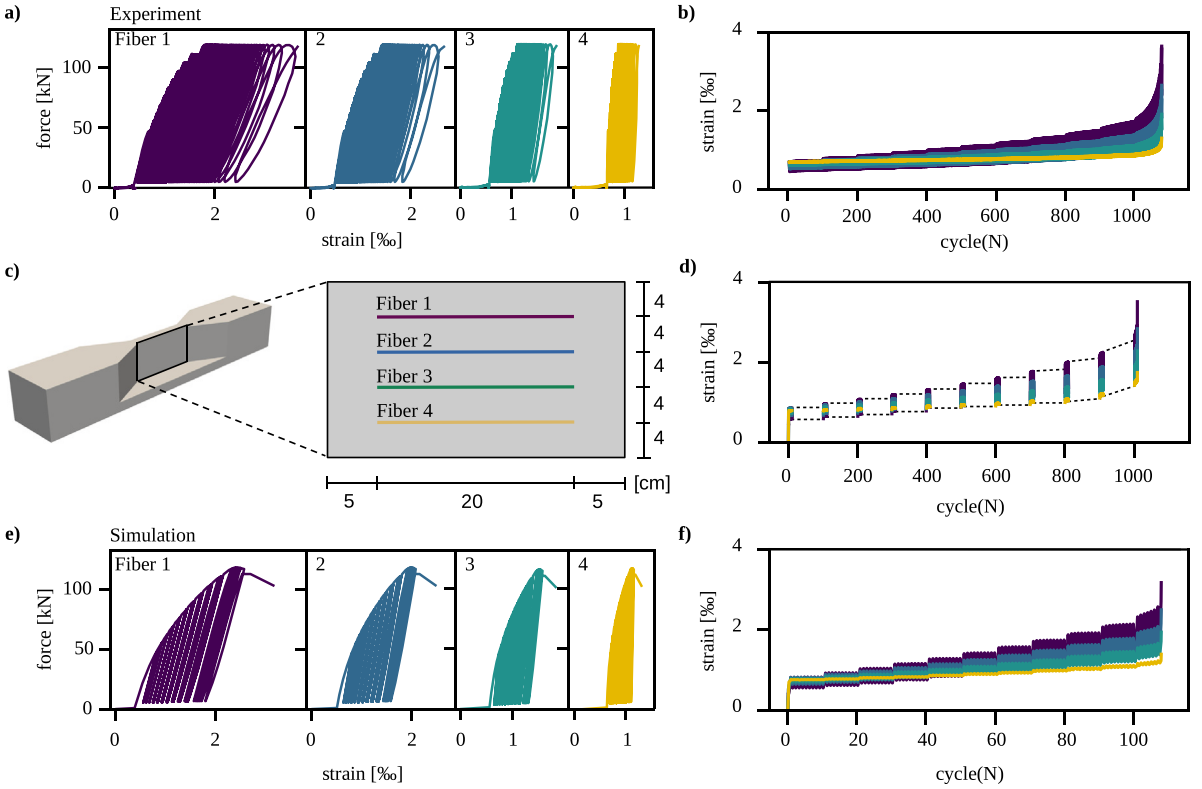


Fig. 13. Experimental validation of the thermodynamically based discrete model for a prestressed concrete beam under four-point bending fatigue loading: (a) and (e) experimental and numerical force–strain curves; (c) beam geometry and fiber sensor locations; (b), (d) and (f) experimental, extrapolated, and simulated fatigue creep curves.

Due to computational constraints, the simulation applied only 10 cycles at each load level, compared to 100 cycles in the experiment. To facilitate meaningful comparison, Fig. 13d presents an extrapolation of the fatigue creep trends obtained from these 10 simulated cycles to the full 100 cycles applied experimentally at each load level. The raw simulation results with 10 cycles per load level are shown in Fig. 13f. At each load level, the strain-rate trend was identified from the last three simulated cycles and extrapolated to predict the strain accumulation during the remaining 90 cycles. The extrapolated response demonstrates that the progression of fatigue-induced strains within each load step is comparable between simulation and experiment, validating the model's ability to capture the degradation kinetics manifested by the deceleration and acceleration of the progressive strain accumulation and by the spatial distribution of damage during the specimen's lifetime. Although the manually calibrated model exhibits a somewhat faster degradation rate — consistent with the S-N curve predictions in Fig. 13a showing shorter lifetimes at lower S_{max} levels — both experiment and simulation fail at the same (tenth) upper load level of S_{max}.

The spatial distribution of energy dissipation under cyclic loading, shown in Fig. 12e, retains the distributed pattern observed in the compression zone during monotonic loading, with no significant quantitative differences. The energy evolution throughout the cyclic loading history, displayed in Fig. 12f, confirms that plasticity remains the dominant mechanism of energy dissipation. Their cumulative effects increase progressively as the cycling advances. A closer examination of the total energy dissipated due to plastic deformation reveals a slight increase in tangential component compared to monotonic loading. This increase can be attributed to inter-aggregate sliding, where the elastic threshold is reached on both sides of the elastic domain during loading and unloading. This observation is particularly relevant for interpreting fatigue tests with uniform subcritical loading, where the interaction between plastic sliding and damage appears to govern the fatigue-induced degradation process.

5.4. Uniform fatigue loading

The model response for the loading scenario LS3 from Table 1 is shown in Fig. 14 for the loading range $S_{max} = 0.9$ and the $S_{min} = 0.04$. Besides the full response in the diagram Fig. 14a, a reduced form of the load–deflection curve is presented in Fig. 14b. The shape of the hysteretic loops reveals the usual evolution during fatigue loading: wider loops at the beginning (stage I) and end (stage III) of the fatigue life and narrower loops during the stabilized phase (stage II). This trend is also reflected in the evaluated evolution of the fatigue-induced deflection in Fig. 14c. In qualitative agreement with the experiments, its shape exhibits the three

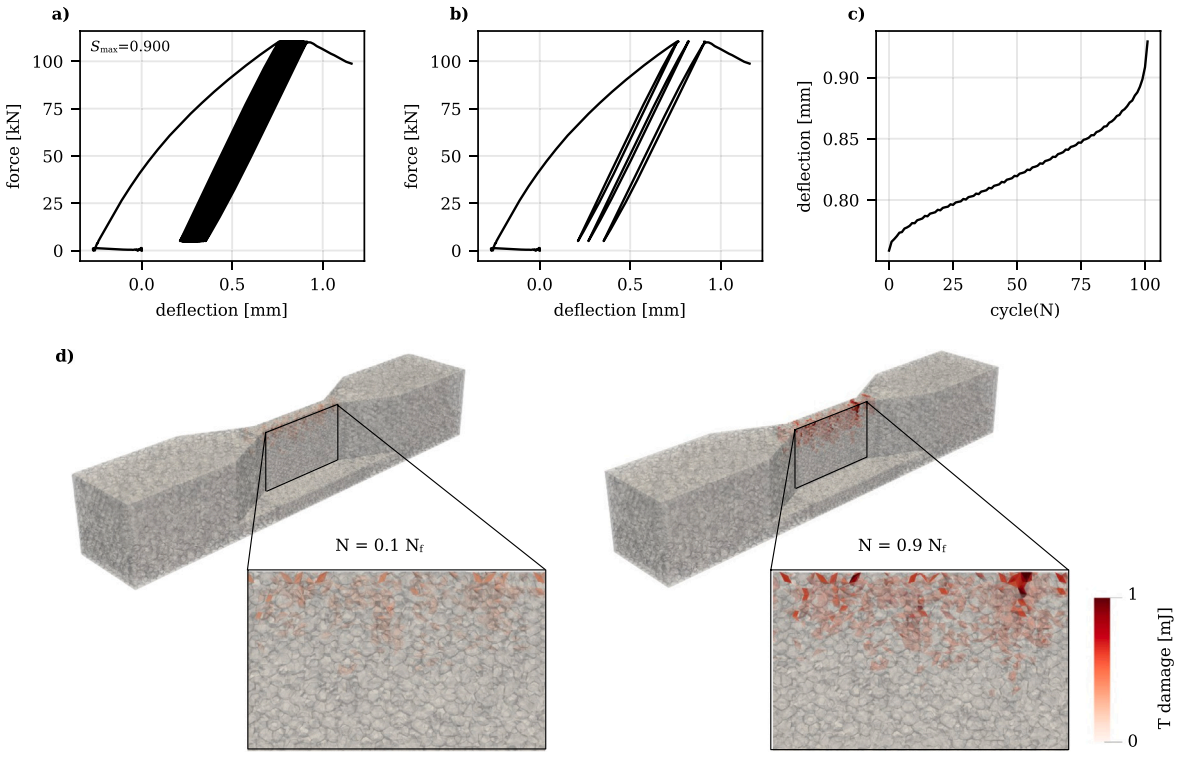


Fig. 14. Simulation of an externally prestressed bending test for $S_{max} = 0.9$: (a) Load–deflection response; (b) Load–deflection response of three selected loading cycles; (c) Corresponding fatigue creep curve; (d) Distribution of tangential damage at 10 and 90% of the fatigue life.

characteristic stages of fatigue behavior: an initial rapid deformation phase, a quasi-linear accumulation phase (stage II), and a final accelerated damage phase leading to failure.

The evolution of damage during fatigue loading, Fig. 14d is visualized in form of tangential damage dissipation at 10% and 90% of the fatigue life. At early stages (0.1 N_f), damage is diffuse and limited, primarily concentrated in the upper part of the beam. As the fatigue process progresses, damage accumulates, propagating downwards and localizing significantly in the same region, eventually leading to failure. This damage propagation induces stress redistribution, both at the material and at structural scales.

To visualize the effect of stress redistribution, Fig. 15 illustrates the evolution of stress fields distributed over the cross-sectional height for three different values of S_{max} = (0.9, 0.925, 0.95) and S_{min} = 0.04. As shown in Fig. 15b, for $S_{max} = 0.9$, the vertical stress profile changes throughout the fatigue life: the top region of the beam, initially carrying the highest compressive stresses, shows a progressive stress reduction, while stresses in the central region increase. Fig. 15c tracks the corresponding evolution of compressive stresses at six locations marked in Fig. 15a.

Despite the differences in S_{max}, the general pattern of stress redistribution is similar for all three studied cases, as illustrated in Figs. 15d and e. This suggests that, within this high-stress amplitude regime, the mechanism of stress redistribution remains largely unaffected by the particular value of S_{max}.

6. Lifetime scale: engineering fatigue characteristics

6.1. S-N curve

To provide the simulation results in a form relevant for engineering assessment rules for concrete fatigue exposure, the results obtained for the studied values of S_{max} are collected in Fig. 16. The corresponding load–deflection and deflection evolution curves are shown for the studied levels of S_{max} in Figs. 16a–b.

The calculated results enable a direct comparison between the material and structural fatigue performance using the S-N curves displayed in Fig. 16c. The S-N values obtained for the prestressed bending test (empty circles) are compared with the dashed S-N line specified for uniaxial-compression fatigue in Model Code 2010 [77] and with the simulations on prisms (solid circles) described in Section 4.2. Apparently, the S-N points for the prestressed bending test are shifted to the right, indicating a longer fatigue life for the equivalent nominal fatigue load ranges. This shift is attributed primarily to stress redistribution effect over the height of the compression zone of a structural member, as previously discussed in the context of Fig. 15.

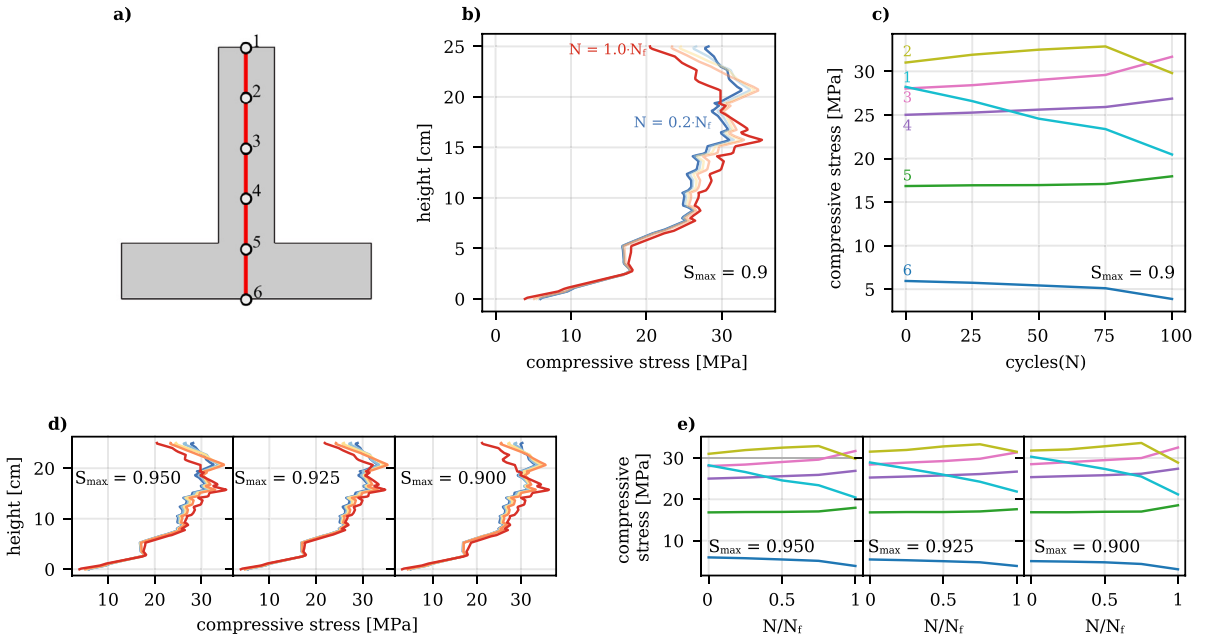


Fig. 15. Stress evolution during fatigue loading for externally prestressed beam simulations. (a) Schematic representation of the cross-section and the six vertical monitoring points used for stress evaluation; (b) Evolution of the stress profile along the beam height at five different points in the fatigue life for $S_{max} = 0.9$; (c) Stress evolution at five selected heights of the cross-section throughout the normalized fatigue life for $S_{max} = 0.9$; (d) Comparison of the vertical stress profiles at different fatigue life stages for $S_{max} = 0.9$, $S_{max} = 0.925$, and $S_{max} = 0.95$; (e) Evolution of stress over fatigue life at five selected heights for the three different S_{max} levels.

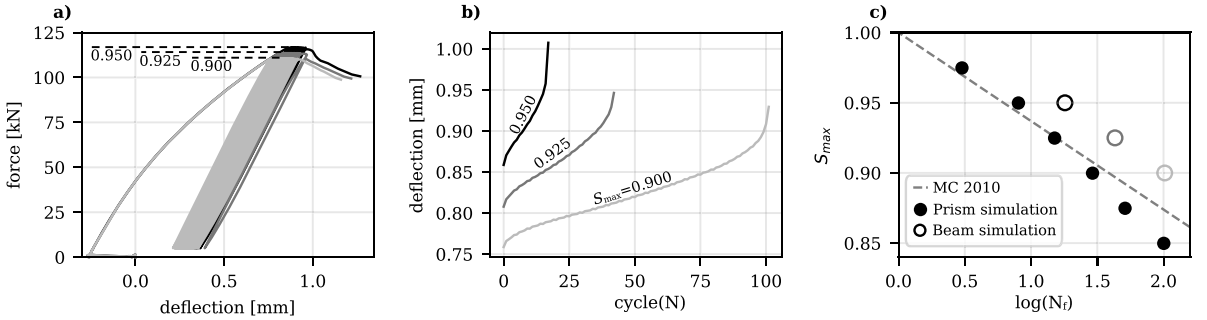


Fig. 16. Structural response of a prestressed bending beam tested at three amplitude levels ($S_{max} = 0.950, 0.925, 0.900$): (a) Force–deflection curves under the different amplitude levels (b) Evolution of deflection over loading cycles. (c) S-N diagram of the prestressed bending test compared with the uniaxial-compression fatigue S-N curve from Model Code 2010.

6.2. Sparks–Menzies relation

Besides S-N curves, the numerical model enables the evaluation of the Sparks–Menzies relation at different positions of horizontal monitoring fibers displayed in Fig. 12a. For each fiber, the strain accumulation rate during the secondary fatigue phase was computed numerically. Additionally, the top fiber with the highest compressive stresses is included in form of black empty circles in Fig. 17f.

The diagram in Fig. 17f deserves a more detailed discussion as it highlights an important general result: The Sparks–Menzies slope numerically obtained for the structural level perfectly follows the trend indicated by the dashed line, which represents the regression of experimental data compiled by Oneschkow from a large set of tests on cylinder specimens [79]. This level of agreement allows the conclusion that the magnitudes of fatigue strain rate and of the number of cycles-to-failure change with the same order, not only at the material level but also at the structural level. This statement can be restated by saying that material structure reveals its ultimate lifetime capacity during the cyclic loading via the observable rate of increasing deformation in the most critical section.

Let us note, that the logarithmic link between the two fatigue characteristics, i.e., fatigue strain rate and lifetime, persists independently on the fatigue load level and boundary conditions. Further, regarding the Sparks–Menzies slope, there is no difference between the material and structural level, all points are positioned on the dashed line. This possibility to integrate the strain

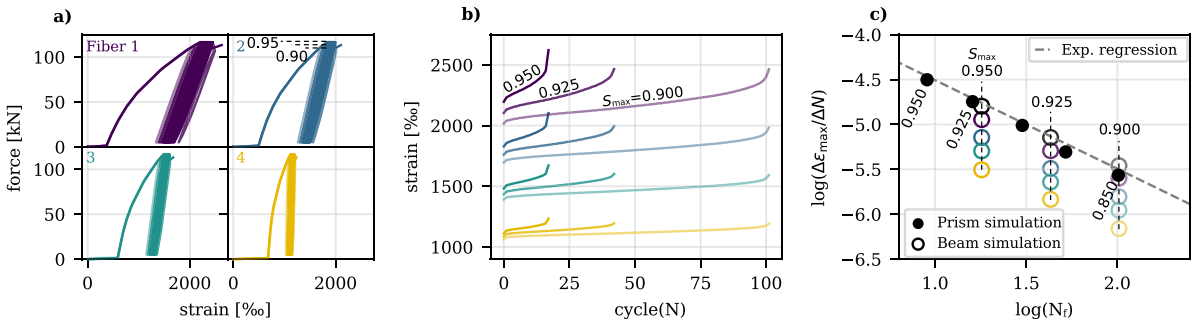


Fig. 17. Structural response of a prestressed bending beam tested at three amplitude levels (S_{max} = 0.950, 0.925, 0.900): (a) Force-strain curves at the four measurement positions along the beam height, as indicated in Fig. 13. (b) Strain evolution at these positions. (c) Comparison of (i) simulated strain rate during secondary phase at the four described positions, plus at the beam top fibre in black (empty circles), (ii) regression based Sparks–Menzies relation based on experimental campaign – Eq. (6.6) in [79], (iii) uniaxial compression simulations of prisms (filled circles) from Fig. 6.

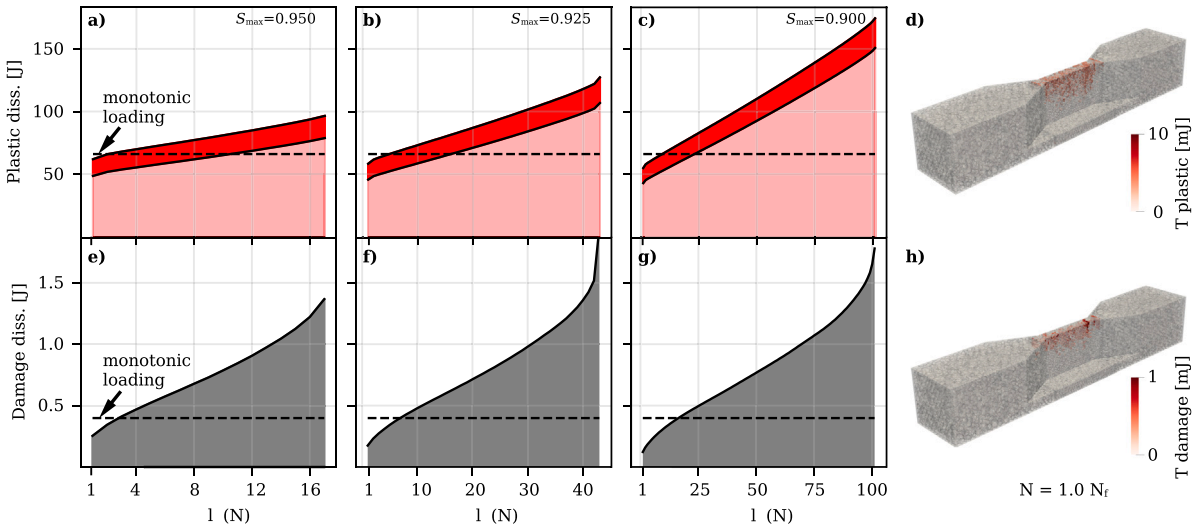


Fig. 18. Breakdown of energy dissipation in each fatigue simulation compared to the reference monotonic loading case (dashed line). (a)–(c) Evolution of plastic dissipation over the number of cycles for the conducted simulations. (d) Spatial distribution of plastic dissipation across lattice facets at failure. Second row: (e)–(g) Evolution of damage dissipation over the number of cycles. (h) Spatial distribution of damage dissipation (normal and tangential) at failure.

accumulation rates measured at the most critical regions of a structure makes the Sparks–Menzies slope a suitable fatigue degradation indicator in structural health monitoring.

On the other hand, considering the individual load levels S_{max}, with the corresponding Sparks–Menzies values positioned along the dashed line in Fig. 17c, we can identify a significant shift between the results obtained for prisms (filled circles), and for the prestressed beams (empty circles). This shift is attributed to the stress redistribution effect in the structural member, which indicates slower strain rate and longer lifetime magnitudes.

6.3. Dissipative behavior

After discussing the potential meaning of the Sparks–Menzies slope as a geometry- and load-independent material property, let us investigate another candidate for an energetically based objective fatigue characteristic: the total damage-induced energy dissipation. Fig. 18 presents the evolutions and final spatial distribution patterns of energy dissipation for the three studied levels of S_{max}. While the total plastic dissipation shown in the top row scales with the number of conducted load cycles-to-failure, the total damage dissipation remains at the same niveau for all three levels. To visualize the effect of fatigue loading on the amount of the energy dissipation, the dashed horizontal lines in Fig. 18 show also the magnitude of energy dissipated for monotonic loading up to peak load. Due to the microstructural stress redistribution during the fatigue loading, the amount of inter-aggregate facets

contributing to the overall dissipation will be larger compared to monotonic loading. As a consequence the size of the dissipating volume, and the overall damage dissipation will be larger for fatigue loading than for monotonic loading.

The comparison of studies shown in Figs. 7 and 18 allows us to posit a hypothesis regarding the energetic characterization of concrete fatigue degradation under compressive subcritical loading. A key observation emerges from both the prism and beam simulations: while the total damage dissipation varies with specimen geometry (0.4 J for prisms, 1.2 J for beams), it exhibits remarkable consistency with respect to the applied loading level $S_{\max}$ within each geometry. As demonstrated in Figs. 7e–h and 18e–g, the total damage dissipation at failure remains approximately constant across the studied range of $S_{\max} \in [0.80, 0.975]$ for prisms and $S_{\max} \in [0.90, 0.95]$ for beams, despite the number of cycles to failure varying by more than an order of magnitude. This load-level independence suggests that damage dissipation capacity might be interpreted as an exhaustible material property governed by the stress configuration rather than the loading amplitude—in contrast to plastic dissipation, which scales with the number of loading cycles and depends on the specific fatigue scenario.

The three-fold difference in total damage dissipation between prism and beam tests appears to scale with the ratio of their respective dissipative volumes, suggesting a specific damage dissipation capacity as a volumetric material property. The prism volume is $100 \times 50 \times 50 = 250{,}000$ mm^3, while the effective compression zone in the beam — estimated from the region where significant damage accumulates — has dimensions approximately $200 \times 50 \times (70\text{–}100)$ mm, yielding $700{,}000\text{–}1{,}000{,}000$ mm^3. Normalizing the total damage dissipation by the effective dissipative volume yields a specific damage dissipation capacity of approximately $1.2\text{–}1.6 \times 10^{-6}$ J/mm^3 for the studied compressive fatigue configurations. This finding suggests that, within the compression-dominated stress regime, the material structure possesses a characteristic energy absorption capacity per unit volume that is exhausted during fatigue degradation, independent of the applied fatigue load sequence.

However, this preliminary finding is based on only two geometries, both subjected to compressive stress configurations. The specific damage dissipation capacity identified here is inherently dependent on the particular loading path within the principle stress/strain space. Different stress configurations — such as triaxial compression with varying levels of confinement, or mixed tension-compression states — will exhibit different specific dissipation values as they trigger distinct triaxial stress redistribution patterns within the material structure. Furthermore, the microstructural topology plays a crucial role: in compression, the material zone contains numerous parallel load paths through the aggregate skeleton, promoting homogeneous damage distribution and stable degradation, whereas tensile loading involves more series-type structural links, leading to localization into discrete macrocracks. Establishing a general quantitative relationship between damage dissipation and structural geometry across different stress states would require systematic validation across multiple specimens, loading configurations, and degrees of stress triaxiality. Nevertheless, the observed trend provides a plausible first indication that, for compressive fatigue, damage dissipation might scale with the stressed volume analogous to how fracture energy governs crack propagation in cohesive crack models.

6.4. Model scope, limitations, and future developments

In its current form, the model is not computationally feasible for direct simulation of concrete structures subjected to high-cycle fatigue. Rather than relying on brute-force cycle-by-cycle integration, the model is intended to support the development of high-cycle fatigue prediction strategies through three complementary approaches: (i) predictive cycle jumping combined with adaptive consistency verification against the full model, (ii) extrapolation after the onset of the secondary branch of the fatigue–creep response, coupled with the established Sparks–Menzies slope relationship, and (iii) the formulation of an effective time-homogenized constitutive framework capable of capturing fatigue degradation at accelerated time scales.

Nevertheless, the primary value of the proposed model does not lie in exhaustive simulation of all loading scenarios to extremely high cycle counts, but rather in its ability to:

- provide physically based, mechanistic insight into fatigue processes that cannot be obtained from purely empirical approaches,
- validate and refine constitutive theories through direct comparison with detailed experimental observations, and
- investigate critical scenarios involving complex loading histories and variable-amplitude fatigue, for which empirical models offer limited predictive capability.

As is generally recognized, fatigue life exhibits significant scatter, stemming from multiple sources of randomness. The proposed framework provides a systematic means of introducing relevant sources of variability within the material structure. It has already been shown for monotonic loading that the scatter arising solely from the random placement of rigid bodies in mesoscale discrete models does not reproduce the experimentally observed variability in mechanical response [80], and that the inclusion of additional sources of variability through random material parameters is straightforward [81,82].

7. Conclusions

This paper presents a novel combination of the lattice discrete particle model with thermodynamically based material model focused on concrete fatigue degradation. The constitutive inter-aggregate model has been calibrated using monotonic and cyclic uniaxial compression loading on concrete prisms. The predictive capabilities of the model are demonstrated through the design and analysis of a prestressed four-point bending test specifically developed for investigating structural compressive fatigue. Structural-scale validation is achieved through comparison with experimental strain measurements at multiple beam locations under stepwise increasing cyclic loading, demonstrating the ability of the model to capture stress redistribution and progressive damage evolution. The key findings of this study can be summarized as follows:

Effect of stress-redistribution on the S-N curve. The simulated fatigue life of the prestressed beam is larger compared to that of the prisms. This difference appears as a horizontal shift of the fatigue life of the prestressed beam in the S-N diagram with respect to the curve specified by the fib Model Code 2010 for uniaxial compression, indicating improved fatigue resistance. This confirms that fatigue design based solely on uniaxial compression tests would be overly conservative when directly applied to structural components.

Size of the stress redistribution zone. In the studied range of fatigue load scenarios, the profiles of stress redistribution over the beam depth were almost identical. This observation suggests that averaging of stress profiles, as applied in current assessment rules, is justified. Further studies at lower load levels would be required to draw a general conclusion regarding the size of the stress redistribution zone and its scaling with the loading range or beam depth, thereby supporting the ongoing development of empirically based design codes [77,83].

Alignment with the Sparks–Menzies slope at structural scale. The simulations confirm the Sparks–Menzies relation, linking the rate of fatigue-induced strain with the number of cycles-to-failure. This outcome can be exploited in structural health monitoring concepts to estimate the lifetime of structures, based on the monitored trends in critical zones. In laboratory conditions, improved concepts of fatigue testing can be exploited for the development of more efficient and targeted fatigue test procedures including an online estimation of the test duration.

Energy dissipation mechanisms. The energy dissipation analysis reveals damage dissipation as a load-level independent characteristic of fatigue resistance. Indeed, the studies suggest that specific damage dissipation capacity can be identified for a given concrete material. Similarly to the concept of fracture energy, defining material specific property for mode I and mode II crack propagation, specific damage dissipation capacity might be identified for elementary stress configurations in the principle stress space.

The presented framework advances the computational concrete fatigue modeling by providing a thermodynamically consistent, multiscale approach that bridges material characterization and structural behavior. The model's capacity to predict structural fatigue performance from material-level calibration data offers substantial potential for reducing dependence on costly full-scale experimental programs while enabling more reliable fatigue design of concrete infrastructure. The mesoscale framework can naturally incorporate further effects influencing the structural lifetime, i.e. temperature and humidity.

CRediT authorship contribution statement

Mario Aguilar: Writing – original draft, Visualization, Validation, Software, Methodology, Investigation, Conceptualization. **Miroslav Vořechovský:** Writing – review & editing, Visualization, Supervision, Software, Methodology, Investigation, Funding acquisition, Conceptualization. **Abedulgader Baktheer:** Writing – review & editing, Visualization, Conceptualization. **Rostislav Chudoba:** Writing – review & editing, Supervision, Methodology, Funding acquisition, Conceptualization.

Declaration of Generative AI and AI-assisted technologies in the writing process

During the preparation of this work, the author(s) used ChatGPT (OpenAI) to assist in improving the clarity and conciseness of the language. After using this tool, the author(s) carefully reviewed and edited the content as needed and take full responsibility for the final content of the publication.

Declaration of competing interest

The authors declare that they have no known competing financial interests or personal relationships that could have appeared to influence the work reported in this paper.

Acknowledgments

The first, third, and fourth authors were supported by the German Research Foundation (DFG) in the framework of the research project (ReinfFatCon: Fatigue degradation of reinforced concrete under predominantly compressive loading), project number (533471030). The second author was supported by the Czech Science Foundation, Czechia under project no. GF22-06684K. Additionally, we gratefully acknowledge ES3 Inc. for providing MARS, which significantly contributed to the completion of this research.

Data availability

Data will be made available on request.

References

[1] Hillebrand M, Schmidt M, Wieneke K, Classen M, Hegger J. Investigations on interface shear fatigue of semi-precast slabs with lattice girders. Appl Sci 2021;11(23). http://dx.doi.org/10.3390/app112311196.

[2] Schäfer N, Gudžulić V, Breitenbücher R, Meschke G. Experimental and numerical investigations on high performance SFRC: Cyclic tensile loading and fatigue. Materials 2021;14(24). http://dx.doi.org/10.3390/ma14247593.

[3] Oneschkow N. Fatigue behaviour of high-strength concrete with respect to strain and stiffness. International J Fatigue 2016;87:38–49. http://dx.doi.org/10.1016/j.ijfatigue.2016.01.008.

[4] Miarka P, Seitl S, Bílek V, Cifuentes H. Assessment of fatigue resistance of concrete: S-N curves to the Paris' law curves. Constr Build Mater 2022;341:127811. http://dx.doi.org/10.1016/j.conbuildmat.2022.127811.

[5] Lohaus L, Oneschkow N. Cyclic deterioration of high-performance concrete – findings of the priority programme SPP 2020. Ce/Papers 2023;6(6):833–43. http://dx.doi.org/10.1002/cepa.2834.

[6] Schmidt B, Schneider S, Marx S. Betonermüdung – Sicherheiten und entwicklungspotenziale aktueller nachweiskonzepte. Bautechnik 2019;96(4):329–37. http://dx.doi.org/10.1002/bate.201900003.

[7] Birkner D, Beltrán Gutiérrez RE, Marx S. Comparison of stiffness degradation in fatigue-loaded concrete cylinders and large-scale beams. Eng Struct 2024;302:117360. http://dx.doi.org/10.1016/j.engstruct.2023.117360.

[8] Riyar RL, Mansi, Bhowmik S. Fatigue behaviour of plain and reinforced concrete: A systematic review. Theor Appl Fract Mech 2023;125:103867. http://dx.doi.org/10.1016/j.tafmec.2023.103867.

[9] Baktheer A, Goralski C, Hegger J, Chudoba R. Stress configuration-based classification of current research on fatigue of reinforced and prestressed concrete. Struct Concr 2024. http://dx.doi.org/10.1002/suco.202300667.

[10] Viswanath S, LaFave JM, Kuchma DA. Concrete compressive strain behavior and magnitudes under uniaxial fatigue loading. Constr Build Mater 2021;296:123718. http://dx.doi.org/10.1016/j.conbuildmat.2021.123718.

[11] Schneider S, Vöcker D, Marx S. Zum einfluss der belastungsfrequenz und der spannungsgeschwindigkeit auf die ermüdungsfestigkeit von beton. Beton-Stahlbetonbau. 2012;107(12):836–45. http://dx.doi.org/10.1002/best.201200054.

[12] Elsmeier K, Hümme J, Oneschkow N, Lohaus L. Prüftechnische einflüsse auf das ermüdungsverhalten hochfester feinkörniger vergussbetone. Beton-Stahlbetonbau. 2016;111(4):233–40. http://dx.doi.org/10.1002/best.201500065.

[13] Deutscher M, Tran NL, Scheerer S. Experimental investigations on temperature generation and release of ultra-high performance concrete during fatigue tests. Appl Sci 2020;10(17). http://dx.doi.org/10.3390/app10175845.

[14] Baktheer A, Chudoba R. Experimental study of the interacting effects of loading rate and temperature on concrete fatigue behavior under compression. Constr Build Mater 2025;458:139466. http://dx.doi.org/10.1016/j.conbuildmat.2024.139466.

[15] Abubakar Ali M, Tomann C, Aldakheel F, Mahlbacher M, Noii N, Oneschkow N, Drake K-H, Lohaus L, Wriggers P, Haist M. Influence of moisture content and wet environment on the fatigue behaviour of high-strength concrete. Materials 2022;15(3). http://dx.doi.org/10.3390/ma15031025.

[16] Markert M, Katzmann J, Birtel V, Garrecht H, Steeb H. Investigation of the influence of moisture content on fatigue behaviour of HPC by using DMA and XRCT. Materials 2022;15(1). http://dx.doi.org/10.3390/ma15010091.

[17] Tomann C, Oneschkow N. Influence of moisture content in the microstructure on the fatigue deterioration of high-strength concrete. Struct Concr 2019;20(4):1204–11. http://dx.doi.org/10.1002/suco.201900023.

[18] Aguilar M, Baktheer A, Chudoba R. Multi-axial fatigue of high-strength concrete: Model-enabled interpretation of punch-through shear test response. Eng Fract Mech 2024;311:110532. http://dx.doi.org/10.1016/j.engfracmech.2024.110532.

[19] Becks H, Aguilar M, Chudoba R, Classen M. Characterization of high-strength concrete under monotonic and fatigue mode II loading with actively controlled level of lateral compression. Mater Struct 2022;55(10):252. http://dx.doi.org/10.1617/s11527-022-02087-4.

[20] Becks H, Classen M. New insights into the load sequence effect: Experimental characterization and incremental modeling of plain high-strength concrete under mode II fatigue loading with variable amplitude. Int J Fatigue 2024;185:108334. http://dx.doi.org/10.1016/j.ijfatigue.2024.108334.

[21] Gallwoszus J, Claßen M. Ermüdung von verbunddübelleisten in UHPC unter zyklischer pull-out-beanspruchung. Bautechnik 2015;92(7):509–21. http://dx.doi.org/10.1002/bate.201500020.

[22] Baktheer A, Spartali H, Chudoba R, Hegger J. Concrete splitting and tip-bearing effect in the bond of anchored bars tested under fatigue loading in the push-in mode: An experimental investigation. Mater Struct 2022;55(3):101. http://dx.doi.org/10.1617/s11527-022-01935-7.

[23] Subramaniam KV, Popovics JS, Shah SP. Fatigue fracture of concrete subjected to biaxial stresses in the tensile C-T region. J Eng Mech 2002;128(6):668–76. http://dx.doi.org/10.1061/(ASCE)0733-9399(2002)128:6(668).

[24] Holmen JO. Fatigue of concrete by constant and variable amplitude loading. ACI Spec Publ 1982;75:71–110. http://dx.doi.org/10.14359/6402.

[25] Petkovic G, Lenschow R, Stemland H, Rosseland S. Fatigue of high-strength concrete. Spec Publ 1990;121:505–26. http://dx.doi.org/10.14359/3740.

[26] Hilsdorf HK, et al. Fatigue strength of concrete under varying flexural stresses. In: Journal proceedings. vol. 63, 1966, p. 1059–76.

[27] Baktheer A, Chudoba R. Experimental and theoretical evidence for the load sequence effect in the compressive fatigue behavior of concrete. Mater Struct 2021;54(2). http://dx.doi.org/10.1617/s11527-021-01667-0.

[28] Baktheer A, Camps B, Hegger J, Chudoba R. Numerical and experimental investigations of concrete fatigue behavior exposed to varying loading ranges. In: The 5th international fib congress. (ISBN: 978-1-877040-15-3):2018, p. 1110–23.

[29] Baktheer A, Becks H. Fracture mechanics based interpretation of the load sequence effect in the flexural fatigue behavior of concrete using digital image correlation. Constr Build Mater 2021;307. http://dx.doi.org/10.1016/j.conbuildmat.2021.124817.

[30] Ren W, Deng R, Zhou X-H, Wang Y-H, Cao F, Jin K-Y. Compressive behavior of the steel–concrete composite adapter for wind turbine hybrid towers. Eng Struct 2023;280:115703. http://dx.doi.org/10.1016/j.engstruct.2023.115703.

[31] Palmgren A. Die lebensdauer von kugellagern (durability of ball bearings). ZDVD 1924;68:339.

[32] Miner M, et al. Cumulative fatigue damage. J Appl Mech 1945;12(3):A159–64.

[33] Gudzulic V, Daadouch K, Meschke G. Modelling of damage process in concrete under monotonic and cyclic loading. In: 11th international conference on fracture mechanics of concrete. http://dx.doi.org/10.21012/FC11.092312.

[34] Alrayes O, Könke C, Ooi ET, Hamdia KM. Modeling cyclic crack propagation in concrete using the scaled boundary finite element method coupled with the cumulative damage-plasticity constitutive law. Materials 2023;16(2). http://dx.doi.org/10.3390/ma16020863.

[35] Zhou R, Lu Y, Wang W, Cheng C, Lu Z. Mesoscale modelling of the dynamic tensile strength enhancement of concrete in spalling tests using interface elements. Eng Fract Mech 2024;295:109808. http://dx.doi.org/10.1016/j.engfracmech.2023.109808.

[36] Baktheer A, Martínez-Pañeda E, Aldakheel F. Phase field cohesive zone modeling for fatigue crack propagation in quasi-brittle materials. Comput Methods Appl Mech Engrg 2024;422:116834. http://dx.doi.org/10.1016/j.cma.2024.116834.

[37] Xiong Z, Liu X, Li J, Baktheer A, Wolters K, Feldmann M. An accelerated phase-field model for high-cycle fatigue behaviour in quasi-brittle materials. Theor Appl Fract Mech 2025;139:105003. http://dx.doi.org/10.1016/j.tafmec.2025.105003.

[38] Kirane K, Bažant ZP. Microplane damage model for fatigue of quasibrittle materials: Sub-critical crack growth, lifetime and residual strength. Int J Fatigue 2015;70:93–105. http://dx.doi.org/10.1016/j.ijfatigue.2014.08.012.

[39] Alliche A. Damage model for fatigue loading of concrete. Int J Fatigue 2004;26(9):915–21. http://dx.doi.org/10.1016/j.ijfatigue.2004.02.006.

[40] Desmorat R, Ragueneau F, Pham H. Continuum damage mechanics for hysteresis and fatigue of quasi-brittle materials and structures. Int J Numer Anal Methods Geomech 2007;31(2):307–29. http://dx.doi.org/10.1002/nag.532, [Accessed 2016-08-03].

[41] Kindrachuk VM, Thiele M, Unger JF. Constitutive modeling of creep-fatigue interaction for normal strength concrete under compression. Int J Fatigue 2015;78:81–94. http://dx.doi.org/10.1016/j.ijfatigue.2015.03.026.

[42] Oneschkow N, Timmermann T, Löhnert S. Compressive fatigue behaviour of high-strength concrete and mortar: Experimental investigations and computational modelling. Materials 2022;15(1). http://dx.doi.org/10.3390/ma15010319.

[43] Baktheer A, Chudoba R. Classification and evaluation of phenomenological numerical models for concrete fatigue behavior under compression. Construction Build Materials 2019;221:661–77. http://dx.doi.org/10.1016/j.conbuildmat.2019.06.022.

[44] Baktheer A, Aguilar M, Chudoba R. Microplane fatigue model MS1 for plain concrete under compression with damage evolution driven by cumulative inelastic shear strain. Int J Plast 2021;143. http://dx.doi.org/10.1016/j.ijplas.2021.102950.

[45] Cusatis G, Pelessone D, Mencarelli A. Lattice discrete particle model (LDPM) for failure behavior of concrete. I: Theory. Cem Concr Compos 2011;33(9):881–90. http://dx.doi.org/10.1016/j.cemconcomp.2011.02.011.

[46] Rybczyński S, Dosta M, Schaan G, Ritter M, Schmidt-Döhl F. Numerical study on the mechanical behavior of ultrahigh performance concrete using a three-phase discrete element model. Struct Concr 2022;23(1):548–63. http://dx.doi.org/10.1002/suco.202000435.

[47] Bolander JE, Eliáš J, Cusatis G, Nagai K. Discrete mechanical models of concrete fracture. Eng Fract Mech 2021;257:108030. http://dx.doi.org/10.1016/j.engfracmech.2021.108030.

[48] Cusatis G, Pelessone D, Mencarelli A. Lattice discrete particle model (LDPM) for failure behavior of concrete. I: Theory. Cement Concr Composites 2011;33(9):881–90. http://dx.doi.org/10.1016/j.cemconcomp.2011.02.011.

[49] Cusatis G, Mencarelli A, Pelessone D, Baylot J. Lattice Discrete Particle Model (LDPM) for failure behavior of concrete. II: Calibration and validation. Cem Concr Compos 2011;33(9):891–905. http://dx.doi.org/10.1016/j.cemconcomp.2011.02.010.

[50] Alnaggar M, Cusatis G, Di Luzio G. Lattice discrete particle modeling (LDPM) of alkali silica reaction (ASR) deterioration of concrete structures. Cem Concr Compos 2013;41:45–59. http://dx.doi.org/10.1016/j.cemconcomp.2013.04.015.

[51] Wang J, Vorel J, Botte W, Pelessone D, Wan-Wendner R. Efficient approaches for modeling and simulating the mechanical behavior of concrete using lattice discrete particle models. Comput Struct 2024;305:107557. http://dx.doi.org/10.1016/j.compstruc.2024.107557.

[52] Kawai T. New discrete models and their application to seismic response analysis of structures. Nuclear Eng Design 1978;48(1):207–29. http://dx.doi.org/10.1016/0029-5493(78)90217-0, Special Issue Structural Mechanics in Reactor Technology - Smirt-4.

[53] Cusatis G, Bažant Z, Cedolin L. Confinement-shear lattice CSL model for fracture propagation in concrete. Comput Methods Appl Mech Engrg 2006;195(52):7154–71. http://dx.doi.org/10.1016/j.cma.2005.04.019.

[54] Cusatis G. Strain-rate effects on concrete behavior. Int J Impact Eng 2011;38(4):162–70. http://dx.doi.org/10.1016/j.ijimpeng.2010.10.030.

[55] Smith J, Cusatis G, Pelessone D, Landis E, O'Daniel J, Baylot J. Discrete modeling of ultra-high-performance concrete with application to projectile penetration. Int J Impact Eng 2014;65:13–32. http://dx.doi.org/10.1016/j.ijimpeng.2013.10.008.

[56] Baktheer A, Classen M. A review of recent trends and challenges in numerical modeling of the anisotropic behavior of hardened 3D printed concrete. Addit Manuf 2024;89:104309. http://dx.doi.org/10.1016/j.addma.2024.104309.

[57] Troemner M, Ramyar E, Meehan J, Johnson B, Goudarzi N, Cusatis G. A 3D-printing centered approach to mars habitat architecture and fabrication. J Aerosp Eng 2022;35(1):04021109. http://dx.doi.org/10.1061/(ASCE)AS.1943-5525.0001359.

[58] Eliáš J, Le J-L. Modeling of mode-i fatigue crack growth in quasibrittle structures under cyclic compression. Engineering Fract Mechanics 2012;96:26–36. http://dx.doi.org/10.1016/j.engfracmech.2012.06.019.

[59] Zhu Z, Pathirage M, Wang W, Troemner M, Cusatis G. Lattice discrete particle modeling of concrete under cyclic tension–compression with multi-axial confinement. Constr Build Mater 2022;352:128985. http://dx.doi.org/10.1016/j.conbuildmat.2022.128985.

[60] N. Ueda HO. Quasi-visco-elasto-plastic constitutive model of concrete for fatigue simulation. In: International conference on fracture mechanics of concrete and concrete structures. 2019, http://dx.doi.org/10.21012/FC10.233513.

[61] Le VT, Tran KM, Kodikara J, Bodin D, Grenfell J, Bui HH. A two-surface contact model for DEM and its application to model fatigue crack growth in cemented materials. Int J Plast 2023;166:103650. http://dx.doi.org/10.1016/j.ijplas.2023.103650.

[62] Gong F, Ueda T, Wang Y, Zhang D, Wang Z. Mesoscale simulation of fatigue behavior of concrete materials damaged by freeze-thaw cycles. Constr Build Mater 2017;144:702–16. http://dx.doi.org/10.1016/j.conbuildmat.2017.03.207.

[63] Baktheer A, Chudoba R. Pressure-sensitive bond fatigue model with damage evolution driven by cumulative slip: Thermodynamic formulation and applications to steel-and FRP-concrete bond. Int J Fatigue 2018;113:277–89. http://dx.doi.org/10.1016/j.ijfatigue.2018.04.020.

[64] Chudoba R, Vořechovský M, Aguilar M, Baktheer A. Coupled sliding–decohesion–compression model for a consistent description of monotonic and fatigue behavior of material interfaces. Comput Methods Appl Mech Engrg 2022;398:115259. http://dx.doi.org/10.1016/j.cma.2022.115259.

[65] Birkner D, Marx S. Large-scale fatigue tests on prestressed concrete beams. IABSE Congress – Resilient Technologies for Sustainable Infrastructures; 2021, http://dx.doi.org/10.2749/christchurch.2021.0943.

[66] Becks H, Baktheer A, Marx S, Classen M, Hegger J, Chudoba R. Monitoring concept for the propagation of compressive fatigue in externally prestressed concrete beams using digital image correlation and fiber optic sensors. Fatigue Fract Eng Mater Struct 2023;46(2):514–26. http://dx.doi.org/10.1111/ffe.13881.

[67] Baktheer A, Esfandiari S, Aguilar M, Becks H, Classen M, Chudoba R. Fatigue-induced stress redistribution in prestressed concrete beams modeled using the constitutive hypothesis of inter-aggregate degradation. Fatigue Fract Eng Mater Struct 2024;47(10):3673–92. http://dx.doi.org/10.1111/ffe.14388.

[68] Cibelli A, Wan-Wendner R, Wan-Wendner L, Vorel J, Pelessone D. MARS–a multiphysics framework for the analysis of cast and printed concrete. DBMC 2023 2023. http://dx.doi.org/10.23967/c.dbmc.2023.050.

[69] Wang J, Vorel J, Botte W, Pelessone D, Wan-Wendner R. Adaptive lattice discrete particle model for concrete. Comput Struct 2025;317:107925. http://dx.doi.org/10.1016/j.compstruc.2025.107925.

[70] Baktheer A, Spartali H, Hegger J, Chudoba R. High-cycle fatigue of bond in reinforced high-strength concrete under push-in loading characterized using the modified beam-end test. Cem Concr Compos 2021;118:103978. http://dx.doi.org/10.1016/j.cemconcomp.2021.103978.

[71] Baktheer A, Aguilar M, Hegger J, Chudoba R. Microplane damage plastic model for plain concrete subjected to compressive fatigue loading. In: 10th international conference on fracture mechanics of concrete and concrete structures, fraMCoS-x. 2019, http://dx.doi.org/10.21012/FC10.233196.

[72] Torre-Casanova A, Jason L, Davenne L, Pinelli X. Confinement effects on the steel–concrete bond strength and pull-out failure. Eng Fract Mech 2013;97:92–104. http://dx.doi.org/10.1016/j.engfracmech.2012.10.013.

[73] Lindorf A, Curbach M. S–N curves for fatigue of bond in reinforced concrete structures under transverse tension. Eng Struct 2010;32(10):3068–74. http://dx.doi.org/10.1016/j.engstruct.2010.05.025.

[74] Xu F, Wu Z-m, Zheng J-j, Hu Y, Li Q-b. Bond behavior of plain round bars in concrete under complex lateral pressures. ACI Struct J 2014;111(1):15. http://dx.doi.org/10.14359/51686427.

[75] Mousavi SS, Guizani L, Ouellet-Plamondon CM. On bond-slip response and development length of steel bars in pre-cracked concrete. Construction Build Materials 2019;199:560–73. http://dx.doi.org/10.1016/j.conbuildmat.2018.12.039.

[76] Yang H, Sinha SK, Feng Y, McCallen DB, Jeremić B. Energy dissipation analysis of elastic–plastic materials. Computer Methods Appl Mech Engineering 2018;331:309–26. http://dx.doi.org/10.1016/j.cma.2017.11.009.

[77] fib – International Federation for Structural Concrete. Fib model code for concrete structures 2010. 2013, http://dx.doi.org/10.1002/9783433604090.
[78] von der Haar C, Marx S. Development of stiffness and ultrasonic pulse velocity of fatigue loaded concrete. Struct Concr 2016;17(4):630–6. http://dx.doi.org/10.1002/suco.201600007.
[79] Oneschkow N. Analyse des Ermüdungsverhaltens von Beton anhand der Dehnungsentwicklung. Hannover: Leibniz Universität Hannover. Institut für Baustoffe; 2014, http://dx.doi.org/10.15488/357.
[80] Eliáš J, Vořechovský M, Skoček J, Bažant Z. Stochastic discrete meso-scale simulations of concrete fracture: Comparison to experimental data. Eng Fract Mech 2015;135:1–16. http://dx.doi.org/10.1016/j.engfracmech.2015.01.004.
[81] Eliáš J, Vořechovský M. Fracture in random quasibrittle media: I. Discrete meso-scale simulations of load capacity and fracture process zone. Engineering Fract Mechanics 2020;235:107160. http://dx.doi.org/10.1016/j.engfracmech.2020.107160.
[82] Vořechovský M, Eliáš J. Fracture in random quasibrittle media: II. Analytical model based on extremes of averaging process. Engineering Fract Mechanics 2020;235:107155. http://dx.doi.org/10.1016/j.engfracmech.2020.107155.
[83] Ríos C, Lancha J, Vicente M. La fatiga en hormigón estructural según el nuevo eurocódigo 2. Hormigón Y Acero 2023;74(299–300):109–22. http://dx.doi.org/10.33586/hya.2023.3100.